Calculation of the Breit-Rosenthal Effect in the $6p^2\ {}^3P_{1,2},{}^1D_2$ and $6p7s\ {}^3P_1$ states in Pb I

Martin Kinden Karlsen

June 2023

Abstract

The differential Breit-Rosenthal (BR) effect was calculated for the $6p^2\,^3P_{1,2}$ and $^1D_2$, and $6p7s\,^3P_1$ states in Pb I. The mean squared radius $\langle r_n^2 \rangle$ of the nuclear Fermi charge distribution was varied by between $-1.466(\text{fm})^2$ and $+0.779(\text{fm})^2$ from the ^{207}Pb reference isotope, accounting for the whole isotope range[1]. A linear fit $\lambda \langle r_n^2 \rangle$ was made with the results, where the proportionality constants in units of $\%\text{fm}^{-2}$ were estimated to be $\lambda(6p^2\,^3P_1) = -0.083(2)$, $\lambda(6p^2\,^3P_2) = -0.009(4)$, $\lambda(6p^2\,^1D_2) = 0.09(2)$ and $\lambda(6p7s\,^3P_1) = -0.065(3)$. Calculations were done based on multiple CSF expansions of various sizes, and the results indicate that large, computationally expensive computations are not necessary in calculations of the BR effect, as long as proper convergence towards the experimental hyperfine structure constant A has been achieved in the reference isotope.

In addition, calculations varying the nuclear skin thickness by ± 0.1fm and $+0.2$fm from the default value 2.3fm were done. These deviations correspond to one and two standard deviations in the skin thickness obtained by fitting to scattering data [3, p. 31-36]. Resulting deviations in the calculated hyperfine structure constant A were found to be of order 1% of the BR effect for all states. Moreover, the calculated λ-values varied by an order of magnitude or more less than the uncertainty in the determination of λ. The results strengthen the belief that the skin thickness does not affect the BR effect much, as long as the skin thickness is fairly similar between isotopes, indicating that the linear fit $\lambda \langle r_n^2 \rangle$ approximates the BR-effect well.

All calculations were done with the GRASP2018 [5] software package, using an extended grid as recommended for heavy elements by [4] and [12]. Some identical calculations were done with both the extended and default grid, and similar results obtained, indicating that the computationally cheaper default grid may be sufficient for hyperfine anomaly calculations in heavy elements.

Contents

Chapter 1

Introduction

1.1   Motivation and Background

Atoms are basic building blocks of matter, consisting of a nucleus of protons and neutrons, and a cloud of electrons surrounding it. The electrons are confined to be in certain energy states with discrete energy levels, as described by quantum mechanics. When interacting with electromagnetic radiation the atom may absorb or emit energy only in certain discrete quantities, corresponding to electrons moving between the allowed energy levels. The allowed energy transitions depend on the characteristics of the nucleus and electron cloud, leading to unique lines in the absorption and emission spectra for each type of atom. Study of atomic spectra can thus be used to identify elements and analyze their properties. Such study plays a fundamental role in understanding the properties and behavior of matter at the atomic and molecular levels, for example in astrophysics where it is used to obtain information about the composition and behaviour of celestial objects.

Theoretical calculations based on quantum mechanics can be used to predict the electron configurations, energy levels and various properties of atoms and thus provide insight into the underlying physical principles governing atomic systems, and help interpret the experimentally observed spectra.

One property of interest is the hyperfine structure, which are tiny splittings of the allowed electronic energy levels into several very close lying levels that result from weak electric and magnetic interactions between the nucleus and electrons. These levels can be resolved with high-resolution spectroscopy techniques like nuclear magnetic resonance (NMR). By measuring the hyperfine structure splitting, information about e.g. the nuclear magnetic moment may be extracted. This extraction involves theoretical calculations taking into account the distribution of electric charge and magnetization in the nucleus. The nuclear magnetic moment in the theoretical model is then obtained by fitting to the experimental data.

The nuclear magnetic moment can also be measured directly using NMR.

However, this requires a certain lifetime of the nucleus and is not possible for sufficiently unstable nuclei. It may however, be possible to measure the hyperfine structure of these nuclei using laser spectroscopic methods. Since the hyperfine splittings are directly proportional to the nuclear magnetic dipole moment, these may be used to obtain the latter, when compared to the hyperfine splittings in a stable reference nucleus with known magnetic dipole moment. These comparisons involve taking the ratio between the hyperfine strucure constants A_1 and A_2 of the two nuclei, which cannot be done exactly due to the differential hyperfine anomaly, arising due to the different sizes of the nuclei.

The uncertainty this anomaly introduces has traditionally been ignored due to its small order. However, development of technology in laser spectroscopy means that accuracy is now such that the hyperfine anomaly has become significant. Some of the uncertainty can be accounted for by calculating a few corrections, including the Breit-Rosenthal (BR) correction due to the extended nuclear charge distribution. These calculations thus improves the accuracy of nuclear magnetic moment determination in unstable nuclei.

1.2 Structure of Thesis

This thesis presents work including calculations of the BR correction to the hyperfine anomaly for the $6p^2\,^3P_{1,2}$ and $^1D_2$, and $6p7s\,^3P_1$ states between ^{207}Pb and other isotopes, as modelled by changing nuclear radius. The many-electron wave function is approximated as a linear combination of configuration state functions (CSFs), which represent important electron configurations. Multiple CSF expansions of varying sizes are used to compute the BR-correction and the results compared to assess the necessity for large, computationally expensive calculations. Furthermore, the effect of varying the nuclear skin thickness is investigated.

Chapter 2 gives an introduction to atomic structure calculations using quantum theory. The impossibility of exact analytical solutions is discussed, and some approximations and numerical methods are introduced. Chapter 3 gives an introduction to the relativistic atomic theory on which the calculations in this thesis are based, particularly the multi-configuration Dirac-Hartree-Fock (MCDHF) method and the configuration interaction (CI) method used in the calculations. Moreover, chapter 4 gives an introduction to the hyperfine structure, particularly the magnetic dipole interaction, and how the hyperfine structure constants may be calculated theoretically, as well as a description of the hyperfine anomaly. Chapter 5 concludes the theory part, with an introduction to the General Relativistic Atomic structure Package 2018 (GRASP2018)[5], used in the computations.

The next chapters considers the computations performed. Chapter 6 concerns the calculation of electronic wave functions in the reference isotope ^{207}Pb. Chapter 7 concerns the parametric study of the Breit-Rosenthal (BR) effect, where the hyperfine structure constants were calculated for different nuclear radii to model the isotope range of lead. Some lessons learned from the work,

particularly the application of GRASP2018 in hyperfine anomaly calculations, are also presented. Conclusions drawn from the results of the study are presented in chapter 8. Finally, the thesis is concluded with a norwegian language summary in chapter 9.

1.3   Unit System

In this thesis, atomic units are used. Here the reduced Planck's constant $\hbar$, the electron rest mass m_e, and charge e and the factor $4\pi\epsilon_0$ are set to 1. The speed of light c becomes $1/\alpha$, where α is the fine-structure constant. The unit for energy is the Hartree (Ha) where Ha$= \hbar^2/(m_e a_0^2)$.

Chapter 2

Non-Relativistic Atomic Theory

Atoms are bound states of a nucleus of protons and neutrons, and electrons surrounding them. The exact quantum state of an atomic electron is commonly specified with a set of quantum numbers. These are the principal quantum number n specifying the energy level, the azimuthal quantum number l specifying the orbital shape, the magnetic quantum number m specifying the orbital orientation and the spin quantum number s specifying the spin. Electrons with the same n are in the same *shell*, electrons with the same nl are in the same *subshell* and electrons with the same nlm are in the same *orbital*. The electron configuration of an atom is given by the notation

$$(n_1 l_1)^{w_1} (n_2 l_2)^{w_2} ... (n_m l_m)^{w_m},$$

where w_i is the number of electrons in the subshell $n_i l_i$. The distribution of electrons in the atom is crucial for understanding atomic properties and chemical behaviour. Electrons tend to occupy the lowest energy levels (ground state), but can be excited to higher energy levels by absorbing energy, leading to temporary excited states.

2.1 Hydrogen

Hydrogen is the simplest atomic system that exists. It is the only atom, and one of very few quantum systems, whose Hamiltonian eigenvalue equation can be solved analytically. Thus exact wave functions can be obtained, and on the whole all effects may be calculated. This may be done by considering the electron moving in the spherically symmetric Coulomb potential $\hat{V}(\mathbf{r}) = -1/r$ of the much heavier proton located at the origin. Expressing the Hamiltonian in spherical coordinates gives

$$\hat{H} = -\frac{1}{2}\frac{\partial^2}{\partial r^2} - \frac{1}{r}\frac{\partial}{\partial r} + \frac{\hat{\mathbf{L}}^2}{2r^2} - \frac{1}{r},$$

where the first two terms of the kinetic energy concerns movement in radial direction while the last term concerns rotation about the origo. This Hamiltonian commutes with both $\hat{\mathbf{L}}^2$ and $\hat{L}_z$ since it has angular dependency only through the angular momentum term. $\mathbf{L}^2$ and L_z are thus constants of motion and there exists simultaneous eigenfunctions of energy, angular momentum squared and angular momentum projection. Such simultaneous eigenfunctions must have the form

$$\psi(r,\theta,\phi) = R(r)Y_{lm}(\theta,\phi).$$

Only the radial wave function $R(r)$ is affected by the potential $\hat{V}(r)$, while the angular part Y_{lm} is identical for all spherically symmetric potentials. By separating the variables in this way it becomes possible to solve the radial and angular parts separately and then combine them. Inserting into the Schrödinger equation $\hat{H}\psi = E\psi$, using the known eigenvalues $l(l+1)$ of $\hat{\mathbf{L}}^2$ and doing a variable shift $u(r) \equiv rR(r)$ yields a one-dimensional radial equation [9, p. 140]

$$-\frac{1}{2}\frac{d^2u}{dr^2} + \left[\frac{l(l+1)}{2}\frac{1}{r^2} - \frac{1}{r}\right]u(r) = Eu(r).$$

This is a second order partial differential equation which can be solved analytically. Doing this yields the exact wave functions of the hydrogen atom [9, p. 152]

$$\psi_{nlm} = \sqrt{\left(\frac{2}{na}\right)^3 \frac{(n-l-1)!}{2n[(n+l)!]^3}}\, e^{-r/na}\left(\frac{2r}{na}\right)^l \left[L_{n-l-1}^{2l+1}\frac{2r}{na}\right]Y_l^m(\theta,\phi).$$

Moreover, the allowed energies are given by the Bohr-formula [9, p. 149]

$$E_n = -\frac{1}{2n^2}, \qquad n = 1,2,3,... \tag{2.1}$$

A complete derivation is provided by e.g. Griffiths [9, p. 145-152]. It is clear that while the wave functions depend on all three quantum numbers, the energies are determined by the principal quantum number n alone. It is easily seen that the ground state energy of hydrogen is $E_1 = -\frac{1}{2}$ Ha.

2.2 Helium

The next simplest atom is helium, which is a three-body system consisting of the nucleus and two electrons. The Hamiltonian of a two-electron system with a point nucleus at the origin is

$$H = \frac{1}{2}\nabla_1^2 + \frac{1}{2}\nabla_2^2 - \frac{Z}{r_1} - \frac{Z}{r_2} + \frac{1}{r_{12}},$$

with $Z = 2$ for helium. Here $r_{12} \equiv |\mathbf{r}_1 - \mathbf{r}_2|$ is the distance between electron 1 and 2, and the term $1/r_{12}$ is the Coulomb potential energy between electrons i and j in atomic units. If the electron-electron repulsion is disregarded, each electron in helium can have a binding energy of maximum 2 Ha, equal to $Z^2 = 4$ times the ionisation energy $\frac{1}{2}$ Ha for hydrogen, yielding the minimum energy -4 Ha.

However, with the electron-electron interaction included the Hamiltonian is non-separable, and as a result no product solutions on the form $\Psi(\mathbf{r}_1, \mathbf{r}_2) = \psi_1(\mathbf{r}_1)\psi_2(\mathbf{r}_2)$ can be found. This means that the eigenvalue equation

$$H = \left[\frac{1}{2}\nabla_1^2 + \frac{1}{2}\nabla_2^2 - \frac{2}{r_1} - \frac{2}{r_2} + \frac{1}{r_{12}}\right]\Psi(\mathbf{r}_1, \mathbf{r}_2) = E\Psi(\mathbf{r}_1, \mathbf{r}_2),$$

cannot be separated into smaller, individually solvable constituents. In fact even the classical three-body problem, e.g. a star with two planets mutually attracted by gravity and with initial positions and velocities known, has no general analytical solution.

2.3 Many-Particle Atoms

For atoms with $Z > 2$ electrons, finding exact eigenfunctions and eigenenergies is even more hopeless than for helium. Instead one must resort to approximations and numerical solutions. In the following, a few such methods are discussed.

2.3.1 Variational Method

Approximate eigenfunctions and eigenenergies may be obtained by choosing a trial wavefunction $|\psi(\alpha)\rangle$, where α is a variational parameter, and minimizing the energy functional, i.e. setting $\delta E(\psi) = 0$ under variations of the parameter α. Here

$$E(\alpha) = \frac{\langle\psi|\hat{H}|\psi\rangle}{\langle\psi|\psi\rangle} \geq E_0,$$

is the expectational value of the energy in the state $|\psi\rangle$, which for any state is larger or equal to the ground state energy E_0. The resulting parameter that minimize the energy gives an approximation to the true wave function, and the corresponding energy is an upper bound to the true energy.

As an example the ground state energy of hydrogen, $E_{nlm} = E_{100}$ is obtained. The wave function of the hydrogen ground state is spherically symmetric, has no nodes and vanishes as $r \to \infty$. A natural trial function with these properties is

$$\psi(r, \theta, \phi) = e^{-r/\alpha}.$$

The energy is then

$$E(\alpha) = \frac{\langle \psi|\hat{H}|\psi\rangle}{\langle \psi|\psi\rangle} = -\frac{\langle \psi|\frac{1}{2}\nabla^2 + \frac{1}{r}|\psi\rangle}{\langle \psi|\psi\rangle}$$
$$= \frac{1}{2\alpha^2} - \frac{1}{\alpha}.$$

Where it was used that

$$\langle \psi|\psi\rangle = \int_0^\infty 4\pi r^2 e^{-2r/\alpha} dr = \pi\alpha^3$$
$$- \langle \psi|\frac{1}{2}\nabla^2|\psi\rangle = \frac{4\pi}{\alpha^2}\frac{1}{2}\int_0^\infty r^2 e^{-2r/\alpha} dr = \frac{\pi}{2}\alpha$$
$$- \langle \psi|\frac{1}{r}|\psi\rangle = -\int_0^\infty r e^{-2r/\alpha} dr = -\pi\alpha^2.$$

Minimizing the energy with respect to α gives

$$\frac{dE}{d\alpha} = -\frac{1}{\alpha_0^3} + \frac{1}{\alpha_0^2} = 0 \iff \alpha_0 = 1 \implies E(\alpha_0) = -\frac{1}{2},$$

which recovers the exact ground state energy E_1 obtained from the Bohr-Formula in equation 2.1.

2.3.2 Hartree Method

The many-body problem may be simplified into single-particle approximations by assuming independent electrons, such that the wave function of the electronic system can be expressed as a product of the wave functions of the individual electrons:

$$\Psi(\mathbf{r}_1, ..., \mathbf{r}_N) = \prod_{i=1}^N \psi_i(\mathbf{r}_i).$$

The atomic structure is then described by single-particle states (orbitals) ψ_i in an effective potential $\hat{V}(\mathbf{r}_i)$, which consists of the electrostatic attraction from the nucleus, and an effective mean field created by the $N-1$ other electrons. The Pauli exclusion principle is accounted for by all electrons being in different states, although the product wave function is not guaranteed to be anti-symmetric in particle coordinates, which is required to describe physical states. The charge density of electron i is $-|\psi_i(\mathbf{r}_i)|^2$ in atomic units, and thus the potential felt by electron k is

$$\hat{V}(\mathbf{r}_k) = \hat{V}_n(\mathbf{r}_k) + \sum_{i\neq k} \int d\mathbf{r}_i \frac{|\psi_i(\mathbf{r}_i)|^2}{r_{ki}},$$

where $r_{ik} \equiv |\mathbf{r}_i - \mathbf{r}_k|$ and the nuclear potential is $\hat{V}_n(\mathbf{r}_k) = -Z/r_k$ for a point nucleus approximation. Its wave function then satisfies a Schrödinger equation with this potential term:

$$\hat{H}_k \psi_k(\mathbf{r}_k) = \left[-\frac{1}{2}\nabla_k^2 + \hat{V}(\mathbf{r}_k) \right] \psi_k(\mathbf{r}_k) = E_k \psi_k(\mathbf{r}_k).$$

The variational method may be used to find stationary states of the average Hamiltonian $\langle\Psi|\hat{H}|\Psi\rangle$ of the electronic system, with the constraint that the wave function is normalized. In the independent electron picture this means that each electronic wave function has to be normalized:

$$\int d\mathbf{r} |\psi_i(\mathbf{r})|^2 = 1.$$

The expectation value of the Hamiltonian in the product state is

$$\langle\Psi|\hat{H}|\Psi\rangle = \sum_{i=1}^{N} \int d\mathbf{r}_i \psi_i^*(\mathbf{r}_i) \left(-\frac{1}{2}\nabla_i^2 + \hat{V}_n(\mathbf{r}_i) \right) \psi_i(\mathbf{r}_i)$$

$$+ \frac{1}{2} \sum_{i=1}^{N} \sum_{j=1}^{N} \int d\mathbf{r}_i \int d\mathbf{r}_j \psi_i^*(\mathbf{r}_i) \psi_j^*(\mathbf{r}_j) \frac{1}{r_{ij}} \psi_i(\mathbf{r}_i) \psi_j(\mathbf{r}_j).$$

Here the first term represents the kinetic energy of the electrons plus the electron-nucleus interaction, while the second term is the Hartree contribution, also known as the direct contribution, which represents the average Coulomb interaction between the electrons.

Given this expression for the average Hamiltonian, the Lagrange multiplier method may be applied to minimize with the normalization constraints. The energy functional is

$$E\big[\{\psi_i\}; \{\lambda_i\}\big] = \langle\Psi|\hat{H}|\Psi\rangle - \sum_i \lambda_i \left(\int d\mathbf{r}_i |\psi_i(\mathbf{r}_i)|^2 - 1 \right),$$

where $\{\lambda_i\}$ are the Lagrange multipliers. These are multiplied by the constraints that ensure the electronic wave functions are normalized. To obtain the set of orbitals $\{\psi_i\}$ that minimize the total energy, the set of functional derivatives $\{\delta E/\delta\psi_i\}$ and $\{\delta E/\delta\psi_i^*\}$ must be set equal to zero. Here $\delta\psi_i$ and $\delta\psi_i^*$ may be taken as independent variations.

As an example the complex conjugate part of the variation is calculated, starting with the kinetic- and nuclear potential energy term

$$\frac{\delta}{\delta\psi_k^*(\mathbf{r}_k)} \left[\sum_{i=1}^{N} \int d\mathbf{r}_i \psi_i^*(\mathbf{r}_i) \left(-\frac{1}{2}\nabla_i^2 + \hat{V}_n(\mathbf{r}_i) \right) \psi_i(\mathbf{r}_i) \right]$$

$$= \sum_{i=1}^{N} \int d\mathbf{r}_i \delta_{ik} \delta(\mathbf{r}_i - \mathbf{r}_k) \left(-\frac{1}{2}\nabla_i^2 + \hat{V}_n(\mathbf{r}_i) \right) \psi_i(\mathbf{r}_i) = \left(-\frac{1}{2}\nabla_k^2 + \hat{V}_n(\mathbf{r}_k) \right) \psi_k(\mathbf{r}_k),$$

where it was used that $\delta\psi_i^*(\mathbf{r}_i)/\delta\psi_k^*(\mathbf{r}_k) = \delta_{ik}\delta(\mathbf{r}_i - \mathbf{r}_k)$. Moreover, the functional derivative of the direct-contribution is

$$
\frac{\delta}{\delta\psi_k^*(\mathbf{r}_k)}\left[\frac{1}{2}\sum_{i=1}^N\sum_{j=1}^N\int d\mathbf{r}_i\int d\mathbf{r}_j\psi_i^*(\mathbf{r}_i)\psi_j^*(\mathbf{r}_j)\frac{1}{r_{ij}}\psi_i(\mathbf{r}_i)\psi_j(\mathbf{r}_j)\right]
$$

$$
= \frac{1}{2}\sum_{i=1}^N\sum_{j=1}^N\int d\mathbf{r}_i\int d\mathbf{r}_j\delta_{ik}\delta(\mathbf{r}_i - \mathbf{r}_k)\psi_j^*(\mathbf{r}_j)\frac{1}{r_{ij}}\psi_i(\mathbf{r}_i)\psi_j(\mathbf{r}_j)
$$

$$
+ \frac{1}{2}\sum_{i=1}^N\sum_{j=1}^N\int d\mathbf{r}_i\int d\mathbf{r}_j\psi_i^*(\mathbf{r}_i)\delta_{jk}\delta(\mathbf{r}_j - \mathbf{r}_k)\frac{1}{r_{ij}}\psi_i(\mathbf{r}_i)\psi_j(\mathbf{r}_j)
$$

$$
= \frac{1}{2}\sum_{j=1}^N\int d\mathbf{r}_j\psi_j^*(\mathbf{r}_j)\frac{1}{r_{kj}}\psi_k(\mathbf{r}_k)\psi_j(\mathbf{r}_j) + \frac{1}{2}\sum_{i=1}^N\int d\mathbf{r}_i\psi_i^*(\mathbf{r}_i)\frac{1}{r_{ik}}\psi_i(\mathbf{r}_i)\psi_k(\mathbf{r}_k)
$$

$$
= \sum_{i=1}^N\int d\mathbf{r}_i\frac{|\psi_i(\mathbf{r}_i)|^2}{r_{ik}}\psi_k(\mathbf{r}_k).
$$

And finally, the Lagrange multiplier terms yield

$$
\frac{\delta}{\delta\psi_k^*}\left[-\sum_{i=1}^N\lambda_i\left(\int d\mathbf{r}_i|\psi_i(\mathbf{r}_i)|^2-1\right)\right] = -\sum_{i=1}^N\lambda_i\int d\mathbf{r}_i\delta_{ik}\delta(\mathbf{r}_i-\mathbf{r}_k)\psi_i(\mathbf{r}_i) = -\lambda_k\psi_k(\mathbf{r}_k).
$$

Putting it all together yields the Hartree equation for electron k:

$$
\left(-\frac{1}{2}\nabla_k^2 + \hat{V}_n(\mathbf{r}_k)\right)\psi_k(\mathbf{r}_k) + \sum_{i=1}^N\int d\mathbf{r}_i\frac{|\psi_i(\mathbf{r}_i)|^2}{r_{ik}}\psi_k(\mathbf{r}_k) - \lambda_k\psi_k(\mathbf{r}_k) = 0.
$$

The N equations can not simply be solved separately, since each solution for one electron changes its orbital, which in turn changes all other orbitals. A self-consistent set of orbitals must be sought, such that when put into the potential they reproduce themselves as solutions. In practice this is done by solving the equations iteratively. Naturally, the orbitals $\{\psi_i\}$ that enter into the expression for the potential energy are not known, so a starting potential must be chosen. The wave functions are then calculated and the new effective potential obtained from the N states with minimized energy, and so on until convergence. Such a computational method is called a self-consistent field (scf) procedure and the resulting set of orbitals is said to be self-consistent.

2.3.3 Hartree-Fock Method

The Hartree method may be extended to the Hartree-Fock (HF) method by forcing the N-electron wave function to have correct anti-symmetry in the particle coordinates. Again the independent electron picture is considered, and

the Schrödinger equation is approximated as a set of single-particle PDEs. The anti-symmetry requirement can be satisfied by assuming the exact N-body wave function can be approximated by a Slater determinant of N-spin orbitals

$$\psi(\mathbf{r}_i, ..., \mathbf{r}_N) = \frac{1}{\sqrt{N!}} \begin{vmatrix} \psi_1(\mathbf{r}_i) & \psi_1(\mathbf{r}_j) & \dots & \psi_1(\mathbf{r}_N) \\ \psi_2(\mathbf{r}_i) & \psi_2(\mathbf{r}_j) & \dots & \psi_2(\mathbf{r}_N) \\ \vdots & \vdots & \ddots & \vdots \\ \psi_N(\mathbf{r}_i) & \psi_N(\mathbf{r}_j) & \dots & \psi_N(\mathbf{r}_N) \end{vmatrix}.$$

where $\frac{1}{\sqrt{N!}}$ is a normalization factor. The Slater determinant wave function has a few properties. If two electron coordinates are exchanged, then two columns are interchanged, and interchange of two columns in a determinant gives sign change. The slater determinant thus ensures that the wave function is anti-symmetric under exchange of two particle coordinates. Furthermore, if two of the one-particle states are identical, e.g. $\psi_1 = \psi_2$, then two lines in the determinant will be identical, and a determinant with two identical lines is zero. This ensures the Pauli exclusion principle is satisfied: two fermions cannot be in the same one-particle state.

With the Slater determinant wave function the following expression for the average Hamiltonian is obtained

$$\langle \Psi | \hat{H} | \Psi \rangle = \sum_{i=1}^{N} \int d\mathbf{r}_i \psi_i^*(\mathbf{r}_i) \left(-\frac{1}{2} \nabla_i^2 + \hat{V}_n(\mathbf{r}_i) \right) \psi_i(\mathbf{r}_i)$$

$$+ \frac{1}{2} \sum_{i=1}^{N} \sum_{j=1}^{N} \int d\mathbf{r}_i \int d\mathbf{r}_j \psi_i^*(\mathbf{r}_i) \psi_j^*(\mathbf{r}_j) \frac{1}{r_{ij}} \psi_i(\mathbf{r}_i) \psi_j(\mathbf{r}_j)$$

$$- \frac{1}{2} \sum_{i=1}^{N} \sum_{j=1}^{N} \int d\mathbf{r}_i \int d\mathbf{r}_j \psi_i^*(\mathbf{r}_i) \psi_j^*(\mathbf{r}_j) \frac{1}{r_{ij}} \psi_j(\mathbf{r}_i) \psi_i(\mathbf{r}_j).$$

The first two terms are the same as in the Hartree approximation and the final term is the exchange contribution, a purely quantum mechanical effect, which for fermions is due to the Pauli repulsion caused by the anti-symmetrization requirement.

Stationary states of the average Hamiltonian $\langle \Psi | \hat{H} | \Psi \rangle$ may be obtained with the variational method, subject to the same normalization constraints as for the Hartree approximation. The energy functional will thus be identical to the Hartree method, except for the added exchange term. The functional derivative of the exchange contribution is carried out as

$$\frac{\delta}{\delta\psi_k^*(\mathbf{r}_k)}\left[-\frac{1}{2}\sum_{i=1}^{N}\sum_{j=1}^{N}\int d\mathbf{r}_i \int d\mathbf{r}_j \psi_i^*(\mathbf{r}_i)\psi_j^*(\mathbf{r}_j)\frac{1}{r_{ij}}\psi_j(\mathbf{r}_i)\psi_i(\mathbf{r}_j)\right]$$

$$=-\frac{1}{2}\sum_{i=1}^{N}\sum_{j=1}^{N}\int d\mathbf{r}_i \int d\mathbf{r}_j \delta_{ik}\delta(\mathbf{r}_i-\mathbf{r}_k)\psi_j^*(\mathbf{r}_j)\frac{1}{r_{ij}}\psi_j(\mathbf{r}_i)\psi_i(\mathbf{r}_j)$$

$$-\frac{1}{2}\sum_{i=1}^{N}\sum_{j=1}^{N}\int d\mathbf{r}_i \int d\mathbf{r}_j \psi_i^*(\mathbf{r}_i)\delta_{jk}\delta(\mathbf{r}_j-\mathbf{r}_k)\frac{1}{r_{ij}}\psi_j(\mathbf{r}_i)\psi_i(\mathbf{r}_j)$$

$$=-\frac{1}{2}\sum_{j=1}^{N}\int d\mathbf{r}_j \psi_j^*(\mathbf{r}_j)\frac{1}{r_{kj}}\psi_j(\mathbf{r}_k)\psi_k(\mathbf{r}_j) - \frac{1}{2}\sum_{i=1}^{N}\int d\mathbf{r}_i \psi_i^*(\mathbf{r}_i)\frac{1}{r_{ik}}\psi_k(\mathbf{r}_i)\psi_i(\mathbf{r}_k)$$

$$=-\sum_{i=1}^{N}\int d\mathbf{r}_i \psi_i^*(\mathbf{r}_i)\frac{1}{r_{ik}}\psi_k(\mathbf{r}_i)\psi_i(\mathbf{r}_k).$$

The remaining terms are identical to the results for the Hartree-approximation and thus the Hartree-Fock equations are

$$\left(-\frac{1}{2}\nabla_k^2 + \hat{V}_n(\mathbf{r}_k)\right)\psi_k(\mathbf{r}_k) + \sum_{i=1}^{N}\int d\mathbf{r}_i \frac{|\psi_i(\mathbf{r}_i)|^2}{r_{ik}}\psi_k(\mathbf{r}_k)$$

$$-\sum_{i=1}^{N}\int d\mathbf{r}_i \psi_i^*(\mathbf{r}_i)\frac{1}{r_{ik}}\psi_k(\mathbf{r}_i)\psi_i(\mathbf{r}_k) - \lambda_k\psi_k(\mathbf{r}_k) = 0.$$

As for the Hartree-method, the set of equations must be solved iteratively to obtain a self-consistent set of orbitals. However, even numerically there is usually need for further approximation, e.g. rotational invariance may be assumed such that the spin-angular part is given by spinors and spherical harmonics, leaving only the radial part to be solved.

2.3.4 Electron Correlation

The Hartree- and Hartree-Fock methods are mean-field approximations, which means they neglect many-body correlations between particles. They often give good approximations for systems with weak interactions between particles, but become less accurate for strongly interacting systems. The Hartree-Fock energy E_{HF} is the most accurate that can be obtained within the framework of the independent-particle model, and to exceed it the correlated motion of the electrons must be treated [11, p. 76-77]. The correlation energy may therefore be defined as the difference between the exact energy eigenvalue of the Schrödinger equation, and the approximate Hartree-Fock eigenvalue [6, p. 23]

$$E_{\mathrm{corr}} \equiv E_{\mathrm{exact}} - E_{\mathrm{HF}}.$$

Electron correlation is divided into static and dynamic correlation. Static electron correlation are effects that arise from the long-range electron-electron interactions and the correlation due to the occupation of degenerate or near-degenerate orbitals. It is associated with the long-range rearrangement of the electron cloud [6, p. 23]. Dynamic electron correlation is short range and arises from the singularity of the $1/|\mathbf{r}_i - \mathbf{r}_j|$-term where $\mathbf{r}_i \to \mathbf{r}_j$ [6, p. 23]. It involves the dynamic rearrangement of electrons due to continuous motion and interactions.

Chapter 3

Relativistic Atomic Theory

A treatment based on the Schrödinger equation is valid only in the non-relativistic limit, which suffices to explain empirical observations in certain cases, especially for light elements. However, relativistic effects become increasingly important for heavier elements, where the speeds of the electrons can approach a significant fraction of the speed of light, such that their kinetic energies become comparable to their rest mass energies. As a result, the relativistic effects can significantly affect the atomic properties and spectroscopic data.

The most important relativistic effect in atomic structure computations is the relativistic mass correction, which causes the electron to move faster than predicted by the non-relativistic theory, resulting in a contraction of electron orbitals and an increase in the effective nuclear charge. Another important relativistic effect is the spin-orbit coupling, which arises from the interaction between the motion of the electron and its spin. This effect causes the energy levels of the atom to split into fine structure levels, which can be observed in the atomic spectra.

Rather than being solutions to the Schrödinger equation, the eigenfunctions of half integer spin particles are in the relativistic treatment solutions to the Dirac equation. The one-electron Schrödinger orbitals ψ_i are then replaced by one-electron Dirac orbitals ϕ_i which satisfy the single-particle Dirac equation $\hat{H}_D \phi = E\phi$, where $\hat{H}_D$ is the Dirac Hamiltonian. In atomic units it is given by

$$\hat{H}_D = c\boldsymbol{\alpha}_i \cdot \mathbf{p}_i + \beta_i c^2 + \hat{V}(r), \tag{3.1}$$

where $\boldsymbol{\alpha}$ and β are the Dirac matrices $\alpha_i = \begin{pmatrix} 0 & \sigma_i \\ \sigma_i & 0 \end{pmatrix}$ for $i \in \{1, 2, 3\}$, and $\beta = \begin{pmatrix} I_2 & 0 \\ 0 & -I_2 \end{pmatrix}$. $\mathbf{p}_i = -i\nabla$ is the momentum operator for electron i, and c is the speed of light. The first two terms are the Dirac kinetic energy operators while the last is the potential term. As in the non-relativistic case, no analytic solution to the eigenvalue equation $\hat{H}_D \Phi = E\Phi$ is possible for sufficiently complex many-body systems, and numerical methods must be used.

3.1 Many-Particle Atoms

3.1.1 Central Field Approximation

In the central field approximation each electron is assumed to move independently in a spherically symmetric potential field generated by the nucleus plus an effective central potential field accounting for the average Coulomb repulsion between electrons in the atom. The potential energy of electron i is then given by

$$\hat{V}_i(r_i) = \hat{V}_n(r_i) + \hat{V}_{\text{eff}}(r_i).$$

The effective potential term is derived by averaging the electron-electron interactions over all possible electron configurations. The central field Hamiltonian is

$$\hat{H}_{CF} = \sum_{i=1}^{N} \left[c\boldsymbol{\alpha}_i \cdot \mathbf{p}_i + (\beta_i - I_4)c^2 + \hat{V}_i(r_i) \right].$$

As there are no direct interactions between the electrons, each operator acts on the subspace of a single electron and we are in the independent particle picture. Thus the solutions to the eigenvalue equation can be constructed as product of solutions to the one-electron eigenvalue equations such that

$$|\Phi\rangle = \prod_{i=1}^{N} |\phi_i\rangle.$$

Moreover, the total energy eigenvalue E can be approximated as the sum of the one-electron energy eigenvalues $E = \sum_i E_i$.

The kinetic energy term $c\boldsymbol{\alpha}_i \cdot \mathbf{p}_i$ may be expressed in spherical coordinates as [8, p. 136]

$$c\boldsymbol{\alpha}_i \cdot \mathbf{p}_i = -ic\sigma_r \left(\partial_r + \frac{\hat{K}+1}{r} \right),$$

where $\sigma_r = \boldsymbol{\sigma} \cdot \mathbf{e}_r = \left(\begin{smallmatrix} \cos\theta & \sin\theta e^{-i\phi} \\ \sin\theta e^{+i\phi} & -\cos\theta \end{smallmatrix} \right)$. The operator $\hat{K} = -1 - \boldsymbol{\sigma} \cdot \mathbf{l} = -(1 - \hat{J}^2 - \hat{l}^2 - \hat{s}^2)$ has spherical spinor eigenfunctions with eigenvalues κ [8, p. 133]. The eigenvalue equations for the spherical spinors are then $\hat{K}\Omega_{lsjm} = \kappa\Omega_{lsjm}$, where

$$\kappa = \begin{cases} -(l+1) & \text{for } j = l + \frac{1}{2} \\ l & \text{for } j = l - \frac{1}{2}. \end{cases}$$

Furthermore, in a spherically symmetric potential $\hat{V}(r)$ the solutions to the Dirac equation has the general form of spin-orbitals [7, p. 254]

$$\phi_{nlsjm}(\vec{q}) = \frac{1}{r} \begin{bmatrix} P_{nlj}(r)\Omega_{lsjm}(\theta,\phi) \\ iQ_{nlj}(r)\Omega_{\tilde{l}sjm}(\theta,\phi) \end{bmatrix},$$

16

where $P_{nlj}(r)$ and $Q_{nlj}(r)$ are the large and small components of the radial function, so named since in the non-relativistic limit, the large component tends to dominate, while the small becomes negligible. Moreover, $\Omega_{lsjm}(\theta, \phi)$ are the spinor spherical harmonics which are constructed from the coupling of the spherical harmonics $Y_{lm_l}(\theta, \phi)$ with the spinors $\chi_{\frac{1}{2}, m_s}$ as

$$\Omega_{lsjm}(\theta, \phi) = \sum_{m_l, m_s} \left\langle l, \frac{1}{2}; m_l, m_s \middle| j, m_j \right\rangle Y_{lm_l}(\theta, \phi) \chi_{\frac{1}{2}, m_s}.$$

Here $\left\langle l, \frac{1}{2}; m_l, m_s \middle| j, m \right\rangle$ is the Clebsch-Gordan (CG) coefficient that gives the probability amplitude of spin- and orbital angular momenta $\left| \frac{1}{2}, m_s \right\rangle$ and $|l, m_l\rangle$ coupling to a total angular momentum $|j, m_j\rangle$. Moreover, the spinors are $\chi_{\frac{1}{2}, \frac{1}{2}} = \left(\begin{smallmatrix} 1 \\ 0 \end{smallmatrix} \right)$ and $\chi_{\frac{1}{2}, -\frac{1}{2}} = \left(\begin{smallmatrix} 0 \\ 1 \end{smallmatrix} \right)$. The spin-orbitals are single-electron wave functions that account for both the electron spin and its motion in the nuclear potential.

The spin-orbitals can be rewritten as [7, p. 254]

$$\phi_{n\kappa m}(\vec{q}) = \frac{1}{r} \begin{bmatrix} P_{n\kappa}(r)\Omega_{\kappa m}(\theta, \phi) \\ iQ_{n\kappa}(r)\Omega_{-\kappa m}(\theta, \phi) \end{bmatrix}.$$

The $n\kappa m$ quantum numbers are equivalent to $nljm$, and uniquely describe each Dirac orbital. If a solution to the Dirac equation has this form, then the radial functions $P_{n\kappa}$ and $Q_{n\kappa}$ satisfy the coupled radial equations [11, p. 56]

$$(V(r) - E_{n\kappa})P_{n\kappa}(r) - c \left(\frac{d}{dr} - \frac{\kappa}{r} \right) Q_{n\kappa}(r) = 0,$$

$$c \left(\frac{d}{dr} + \frac{\kappa}{r} \right) P_{n\kappa}(r) + \left(V(r) - 2c^2 - E_{n\kappa} \right) Q_{n\kappa}(r) = 0.$$

The energy level $E_{n\kappa}$ is $(2j+1)-$fold degenerate due to the $(2j+1)$ possible values of m_j for the same $nlj = n\kappa$. The degenerate orbitals constitute a subshell. In the relativistic treatment the electron spin affects the energy such that for each non-relativistic subshell nl with $l \neq 0$, there are two $nlj = n\kappa$ relativistic subshells, where j can take either of the two values $l - \frac{1}{2}$ and $l + \frac{1}{2}$. The notation for the relativistic electron configuration is then

$$(n_1 l_1-)^{w_1-}(n_1 l_1+)^{w_1+}...(n_m l_m-)^{w_m-}(n_m l_m+)^{w_m+},$$

where $n_i l_i \pm$ denotes the subshell with $j_i = l_i \pm \frac{1}{2}$. Frequently, the non-relativistic notation is used even when relativistic theory is considered. The specific relativistic subshells involved then depend on the total angular momentum of the state.

3.1.2 Configuration State Functions

Analogous to the Hartree-Fock wave function, the relativistic N-body wave function can be approximated by a Slater determinant of the one-electron spin-orbitals

$$\Phi(\mathbf{r}_1, ..., \mathbf{r}_N) = \frac{1}{\sqrt{N!}} \begin{vmatrix} \phi_1(\mathbf{r}_1) & \phi_1(\mathbf{r}_2) & \dots & \phi_1(\mathbf{r}_N) \\ \phi_2(\mathbf{r}_1) & \phi_2(\mathbf{r}_2) & \dots & \phi_2(\mathbf{r}_N) \\ \vdots & \vdots & \ddots & \vdots \\ \phi_N(\mathbf{r}_1) & \phi_N(\mathbf{r}_2) & \dots & \phi_N(\mathbf{r}_N) \end{vmatrix}.$$

As in the non-relativistic case, the Slater determinant ensures the wave function is anti-symmetric with respect to the interchange of any two electron coordinates, and that each spin-orbital must be distinct to yield a non-zero wave function.

The total angular momentum J should be conserved in a free atomic system, and therefore the N-body wave function should be an eigenfunction of the total angular momentum squared $\hat{J}^2$ and total angular momentum projection $\hat{J}_z$, with corresponding eigenvalues $J(J+1)$ and M_J. Single Slater determinants are rarely such eigenfunctions. However, eigenfunction may be constructed as linear combinations of Slater determinants with the same set of $n_i \kappa_i$ quantum numbers and different m_i quantum numbers. These are configuration state functions (CSFs)

$$\Phi(\Gamma P J M_J) \equiv |\Gamma P J M_J\rangle,$$

where $P = (-1)^{\sum_i l_i}$ is the parity and Γ represents all other information necessary to uniquely describe the state.

In the relativistic treatment the one-electron spin and orbital angular momenta are intrinsically coupled in the four-component spinors. The total angular momentum J of the electronic system is then obtained by consecutively coupling the one-electron angular momenta: $J = \sum_i j_i = \sum_i (l_i + s_i)$, called jj-coupling. A given combination of angular quantum numbers S, L and J is called a level, and is indicated by a term symbol on the form $^{2S+1}L_J$. Relativistically, only J is a good quantum number, such that eigenstates of $\hat{J}^2$ and $\hat{J}_z$ are generally linear combinations of states with the same J, but different L and S. The term symbol then refers to an eigenstate where $^{2S+1}L_J$ is the most important component. A level has $(2J+1)$ possible microstates, which is the statistical weight of the level.

The CSFs are required to be orthonormal $\langle \Gamma_i P_i J_i M_{J_i} | \Gamma_j P_j J_j M_{J_j} \rangle = \delta_{ij}$, which is ensured if the one-electron spin-orbitals are orthonormal.

3.1.3 Atomic State Functions

Single CSFs correspond to a specific electron configuration and only captures the independent motion of electrons within the assigned orbitals, not electron correlation. However, more accurate approximations to the exact wave functions can be constructed as linear combinations of CSFs. By including CSFs corresponding to a broader range of electron configurations with appropriate weighting, the resulting expansion may incorporate electron correlation effects. In fact, the set of CSFs that can be constructed from a set of one-electron orbitals that span the full one-electron Hilbert space will span the full electronic

Hilbert space. Thus, any eigenstate may be expressed as a linear combination of CSFs. Attaining perfect accuracy this way would generally require an infinite expansion, but arbitrary precision can be reached with a finite number, if the most important CSFs are chosen. Such an expansion is called an atomic state function (ASF) [8, p. 43]:

$$\Psi(\Gamma P J M_J) \equiv |\Gamma P J M_J\rangle = \sum_{i=1}^{N_{csf}} c_{\Gamma_i} |\Gamma_i P J M_J\rangle. \tag{3.2}$$

where N_{csf} is the number of CSFs included in the expansion. The ASF is ensured to be an eigenstate of $\hat{J}^2$ and $\hat{J}_z$ by including only CSFs with the same J and M_J in the expansion. Moreover, to ensure a well defined parity, all CSFs are also required to have the same parity P. The expansion coefficients can be organized in a vector $\mathbf{c}_\Gamma = (c_1, ..., c_{N_{CSF}})^T$ which then represents the state fully in the given CSF basis.

3.2 Multi-Configurational Dirac-Hartree-Fock Method

The Hamiltonian of the N-electron system can be approximated by the Dirac-Coulomb (DC) Hamiltonian, where the one-electron effects are given a full relativistic treatment while the two-electron interactions are described by the Coulomb attraction as in the non-relativistic theory. The DC Hamiltonian is then given by

$$\hat{H}_{\mathrm{DC}} = \sum_{i=1}^{N} \left[c\boldsymbol{\alpha}_i \cdot \mathbf{p}_i + (\beta_i - I_4)c^2 + \hat{V}_n(r_i) \right] + \sum_{i=1}^{N} \sum_{i<j} \frac{1}{r_{ij}},$$

where the one-electron operators are the Dirac Hamiltonian operators from equation 3.1, where the electron rest mass has been subtracted. The most important relativistic effects are the one-electron effects which are thus given a full relativistic treatment. The two electron operators $1/r_{ij}$ are the Coulomb potential energy between electrons i and j, which may receive relativistic corrections later.

If the exact N-electron wave function is approximated by an ASF expanded in a set of known CSFs as in equation 3.2, the approximation is optimized in a scf iteration with the multi-configuration Dirac-Hartree-Fock (MCDHF) equations. Similarly to the non-relativistic Hartree and Hartree-Fock equations discussed in chapter 2, these are obtained by applying the variational principle to the energy functional.

The interaction energies associated with the interactions between CSFs can be used to construct a matrix representation of the Hamiltonian. The energy of the state $|\Gamma J\rangle$ is [13, p. 12]

$$E_{\Gamma J} = \langle \Gamma J M | \hat{H}_{\mathrm{DC}} | \Gamma J M \rangle = \frac{1}{\sqrt{2J+1}} \langle \Gamma J \| \hat{H}_{\mathrm{DC}} \| \Gamma J \rangle = \frac{1}{\sqrt{2J+1}} \mathbf{c}_{\Gamma J}^\dagger \mathbf{H} \, \mathbf{c}_{\Gamma J},$$

where $\mathbf{H}$ is the Hamiltonian matrix with the reduced elements [13, p. 12]

$$H_{\alpha\beta} = \langle \Gamma_\alpha J | | \hat{H}_{\mathrm{DC}} | | \Gamma_\beta J \rangle = \sum_{ab} t_{ab}^{\alpha\beta} I(a,b) + \sum_{abcd;k} v_{abcd;k}^{\alpha\beta} R^k(ab;cd).$$

where $t_{ab}^{\alpha\beta}$ and $v_{abcd;k}^{\alpha\beta}$ are angular coefficients arising from the angular integration associated with the one-electron and two-electron operators in the DC Hamiltonian, respectively. The indices a and b represent the quantum numbers $n_a\kappa_a$ and $n_b\kappa_b$ of the radial orbitals. Moreover, $I(a,b)$ are one-electron radial integrals given by [13, p. 13]

$$I(a,b) = \delta_{\kappa_a\kappa_b} \int_0^\infty \left[P_{n_a\kappa_a}(r)V_n(r)P_{n_b\kappa_b}(r) - cP_{n_a\kappa_a}(r)\left(\frac{d}{dr} - \frac{\kappa}{r}\right)Q_{n_b\kappa_b}(r) \right.$$
$$\left. + cQ_{n_a\kappa_a}(r)\left(\frac{d}{dr} + \frac{\kappa}{r}\right)P_{n_b\kappa_b}(r) + Q_{n_a\kappa_a}(r)\left(V_n(r) - 2c^2\right)Q_{n_b\kappa_b}(r) \right] dr.$$

And, finally $R^k(ab;cd)$ are two-electron radial integrals, so-called Slater integrals [13, p. 13]

$$R^k(ab;cd) = \int_0^\infty \left[P_{n_a\kappa_a}(r)P_{n_c\kappa_c}(r) + Q_{n_a\kappa_a}(r)Q_{n_c\kappa_c}(r) \right] \frac{1}{r} Y^k(bd;r)dr,$$

where $Y^k(ab;r)$ are the relativistic Hartree-functions that describe the electron-electron interaction between orbitals in terms of the radial distance r between them, and the angular momentum quantum number k. These are given by

$$Y^k(ab;r) = r \int_0^\infty \frac{r_<^k}{r_>^{k+1}} \left[P_{n_a\kappa_a}(s)P_{n_b\kappa_b}(s) + Q_{n_a\kappa_a}(s)Q_{n_b\kappa_b}(s) \right] ds,$$

where the $r_<^k$ term represents the smaller of the two radial distances r and s, and $r_>^{k+1}$ the larger. The radial functions are required to be orthonormal. The overlap integral between electrons in orbitals a and b being unity leads to the radial orthonormality condition [13, p. 13]

$$C_{ab} = \int_0^\infty \left[P_{n_a\kappa_a}(r)P_{n_b\kappa_b}(r) + Q_{n_a\kappa_a}(r)Q_{n_b\kappa_b}(r) \right] dr - \delta_{n_an_b} = 0.$$

If multiple states with different total angular momentum J are targeted simultaneously, which is usually the case, the energy functional can be constructed as a statistically weighted average of the states. If N_{ASF} is the number of states, the energy functional becomes [13, p. 13]

$$E\big[\{c_i\},\{P_i\},\{Q_i\}\big] = \frac{\sum_{i=1}^{N_{\mathrm{ASF}}} \sqrt{2J^i+1}\,\langle\Gamma_i J_i|\hat{H}_{DC}|\Gamma_i J_i\rangle}{\sum_{i=1}^{N_{\mathrm{ASF}}}(2J^i+1)} + \sum_{a,b}\delta_{\kappa_a\kappa_b}\lambda_{ab}C_{ab},$$

where in the first term the numerator gives the statistical weight of the states and the denominator normalizes the contribution from the numerator to obtain an average energy. In the second term λ_{ab} represents a matrix of Lagrange multipliers associated with enforcing the orthonormality condition between different orbitals.

To obtain the MCDHF equations the energy functional must be minimized with respect to the variational parameters, which are the set of radial components $\{P_i\}$ and $\{Q_i\}$, and mixing coefficients $\{c_i\}$. Given $\mathbf{c}_{\Gamma J}$, the stationary condition for the radial functions yields [13, p. 13]

$$\omega_a \begin{bmatrix} V(a;r) & -c\left(\frac{d}{dr}-\frac{\kappa_a}{r}\right) \\ c\left(\frac{d}{dr}+\frac{\kappa_a}{r}\right) & V(a;r)-2c^2 \end{bmatrix} \begin{bmatrix} P_{n_a\kappa_a}(r) \\ Q_{n_a\kappa_a}(r) \end{bmatrix} = \sum_b \epsilon_{ab}\delta_{\kappa_a\kappa_b}\begin{bmatrix} P_{n_a\kappa_a}(r) \\ Q_{n_a\kappa_a}(r) \end{bmatrix},$$

where ω_a is the generalized occupation number of orbital a, allowing for fractional occupation, and ϵ_{ab} is an energy parameter related to the Lagrange multipliers. As in the non-relativistic Hartree-Fock method the potential $V(a;r)$ consists of both a nuclear direct contribution and an exchange contribution

$$V(a;r) = V_n(r) + Y(a;r) + \overline{X}(a;r).$$

The MCDHF equations are solved iteratively to obtain a self-consistent set of radial orbitals.

3.3 Configuration Interaction

The expansion coefficients c_{Γ_i} of the ASF are optimized by first diagonalizing the Hamiltonian matrix $\mathbf{H}$ in the basis of the chosen radial functions and updating the coefficients to obtain the eigenvalues and eigenvectors which correspond to the interaction energies and expansion coefficients, respectively. The eigenvalue problem is [13, p. 4]

$$\mathbf{Hc} = E\mathbf{c},$$

where $\mathbf{H}$ is the matrix of the Hamiltonian in the CSF space spanned by the CSFs from which the ASF is contructed. After the final orbital basis is obtained with the scf procedure, the expansion coefficients c_{Γ_i} may be adjusted to account for additional corrections by introducing further terms to the Hamiltonian, beyond the DC approximation.

3.3.1 Breit and QED Corrections

The instantaneous Coulomb interaction is an incomplete description of the electron-electron interactions in relativistic atomic structure. The leading order correction to the Coulomb interaction in the DC Hamiltonian, valid to order α^2, is the transverse photon interaction which is a relativistic correction that accounts for magnetic interactions and retardation effects caused by the finite speed of the exchanged virtual photons. This effect is especially important in systems with high atomic number and nuclear charge, where the electrons experience strong Coulomb interactions. Here the transverse photon interaction can significantly affect the electronic structure and the accuracy of theoretical calculations. The Hamiltonian for the interaction is [4, p. 34]

$$H_T = -\sum_{i<j}^{N} \left[\boldsymbol{\alpha}_i \cdot \boldsymbol{\alpha}_j \frac{\cos(\omega_{ij} r_{ij}/c)}{r_{ij}} + (\boldsymbol{\alpha}_i \cdot \nabla_i)(\boldsymbol{\alpha}_j \cdot \nabla_j) \frac{\cos(\omega_{ij} r_{ij}/c) - 1}{\omega_{ij}^2 r_{ij}/c^2} \right],$$

where ω_{ij} is the angular frequency of the virtual photon exchanged between electrons i and j, assumed to be the difference in orbital energies [4, p. 35]. This is a poor approximation for multiply occupied orbitals and correlation orbitals [4, p. 35], and therefore the correction is often computed in the low-frequency limit by multiplying by a scale factor (often 10^{-6}). In the short frequency limit this reduces to the Breit interaction [6, p. 6]

$$H_{Breit} = -\sum_{i<j}^{N} \frac{1}{2r_{ij}} \left[(\boldsymbol{\alpha}_i \cdot \boldsymbol{\alpha}_j) + \frac{(\boldsymbol{\alpha}_i \cdot \mathbf{r}_{ij})(\boldsymbol{\alpha}_j \cdot \mathbf{r}_{ij})}{r_{ij}^2} \right].$$

Adding this leading order correction to the DC Hamiltonian yields the Dirac-Coulomb-Breit (DCB) Hamiltonian

$$H_{DCB} = H_{DC} + H_{Breit}.$$

Further corrections from quantum electrodynamics (QED) like vacuum polarisation and self-energy can also be added to the Hamiltonian. Vacuum polarisation results from the creation of virtual electron-positron pairs in the vacuum, which modifies the electron energy levels by interacting with them. The self-energy is the energy correction due to interaction with virtual photons emitted and reabsorbed by the electron. The QED corrections are typically small compared to other atomic structure effects, but they become important for high-precision atomic spectroscopy, such as in measurements of the fine- and hyperfine structure.

If such corrections are added to the Hamiltonian in the CI method, it is said to be a relativistic configuration interaction (RCI).

Chapter 4

Hyperfine Structure

The hyperfine interaction arises from the coupling of the magnetic moments of the nuclear- and electronic spin angular momenta. Preferred orientations of electrons are caused by the nuclear magnetic field interacting with the magnetic moment of the electron cloud, breaking the spherical symmetry. This spatial and magnetic structure of the nucleus leads to electromagnetic multipole moments which interact with the electron cloud. These interactions are the hyperfine interactions. The corresponding splittings of the energy levels resulting from these interactions are called hyperfine splittings. The Hamiltonian of the hyperfine interaction can be written as a multipole expansion [8, p. 459]

$$H_{\text{hfs}} = \sum_{k \geq 1} \mathbf{T}^k \cdot \mathbf{M}^k$$

where $\mathbf{T}^k$ and $\mathbf{M}^k$ are rank k spherical tensor operators, which operate on electronic- and nuclear wavefunctions $|\Gamma_j J M_J\rangle$ and $|\Gamma_i I M_I\rangle$, respectively. The $k = 1$ term is the magnetic dipole term and the $k = 2$ term is the electric quadrupole term. Higher order terms can often be neglected.

4.1 Magnetic Dipole Interaction

The electronic magnetic dipole operator in an N-electron atom can be written as a sum over one-electron operators [13, p. 16]

$$\mathbf{T}^{(1)} = \sum_{j=1}^{N} \mathbf{t}^{(1)}(j) = \sum_{j=1}^{N} -i\sqrt{2}\alpha r_j^{-2}\left(\boldsymbol{\alpha}_j \mathbf{C}^{(1)}(\theta_j, \phi_j)\right),$$

where α is the fine structure constant, $\boldsymbol{\alpha}_j$ is a Dirac matrix and $\mathbf{C}^{(1)}$ is a spherical tensor with components $C_q^{(1)} = \sqrt{\frac{4\pi}{3}}Y_{1q}$, where Y_{1q} are the spherical harmonics and $q = 0, \pm 1$. Moreover, the nuclear tensor operator $\mathbf{M}^1 = \vec{\mu}_I$ is related to the nuclear magnetic dipole moment μ_I via

$$\mu_I = \langle \Gamma_i II | \mathbf{M}^{(1)} | \Gamma_i II \rangle .$$

The magnetic dipole moments can generally be experimentally determined with high accuracy.

The total angular momentum of a free atomic system is conserved, and thus the system can be described with stationary eigenstates of $\hat{F}^2$ and $\hat{F}_z$, where $\hat{F} = \hat{I} + \hat{J}$ is the total angular momentum operator of the entire atomic system. Such eigenfunctions are given as coupled wave functions

$$|\Gamma_i \Gamma_j IJFM_F\rangle = \sum_{M_I M_J} \langle IJM_I M_J | IJFM_F \rangle |\Gamma_i IM_I\rangle |\Gamma_j JM_J\rangle , \qquad (4.1)$$

where the Clebsch-Gordan coefficient $\langle IJM_I M_J | IJFM_F \rangle$ gives the probability amplitude of the nuclear state $|\Gamma_i IM_I\rangle$ and the electronic state $|\Gamma_j JM_J\rangle$ coupling to the total state $|\Gamma_i \Gamma_j IJFM_F\rangle$. The eigenvalue of $\hat{F}$ is denoted F.

The hyperfine interaction couples both angular momenta $\vec{I}$ and $\vec{J}$ such that the orientation of $\vec{I}$ is no longer independent of the orientation of $\vec{J}$. This lifts the degeneracy of the energy levels, and yields a dependence on F. F can take any value $|I - J|, |I - J| + 1, ..., I + J$, where each value correspond to a specific orientation of $\vec{I}$ with respect to $\vec{J}$.

If the hyperfine energies are small compared to the fine structure energies, which is usually the case, the interaction can be treated as a first order perturbation, where the zero-order wave functions are given by equation (4.1). Using this the diagonal and off-diagonal magnetic dipole interaction energies between nuclear and electronic basis states are [14, p. 3]

$$E_{\mathrm{M1}}(J, J') = \langle \Gamma_i \Gamma_j IJFM_F | \mathbf{T}^{(1)} \cdot \mathbf{M}^{(1)} | \Gamma_i \Gamma_j IJ'FM_F \rangle ,$$

where $J' = J, J - 1$, accounting for the magnetic dipole nature of the interaction. The diagonal energies describe the interaction within the same electronic state but with different nuclear spin states, while the off-diagonal energies describe the interaction between different electronic states with different nuclear spin states. $\mathbf{T}^{(1)}$ is an irreducible tensorial operator whose matrix elements $\langle \Gamma_j JM_J | T_q^{(k)} | \Gamma_{J'} J'M_{J'} \rangle$ can be factorized via the Wigner-Eckhart theorem. Defining the reduced matrix elements in the Brink and Satchler version of the theorem gives [13, p. 10]

$$\langle \Gamma_j JM_J | T_q^{(k)} | \Gamma_{J'} J'M_{J'} \rangle = (-1)^{J-M_J} \sqrt{2J+1} \begin{Bmatrix} J & k & J' \\ -M_J & q & M_{J'} \end{Bmatrix} \langle \Gamma_j J | |\mathbf{T}^{(k)}| | \Gamma_{J'} J' \rangle ,$$

where $(-1)^{J-M_J}$ is a phase factor that accounts for the transformation properties of the CG coefficients under sign changes of the projection quantum numbers, and $\sqrt{2J+1}$ is a degeneracy factor that arises because there can be multiple states with the same angular momentum J. The 2×3 array is a Wigner $3j$-symbol that relates the coupling of three angular momenta to form

a fourth angular momentum. The matrix elements of the irreducible operator are thus expressed as a product of a $3j$-symbol and the reduced matrix element $\langle \Gamma_j J | |\mathbf{T}^{(k)}| |\Gamma_{J'} J' \rangle$ which is simply a proportionality factor independent of $M_J, M_{J'}$ and q. This makes it possible to relate matrix elements of complex operators to simpler operators, greatly simplifying calculations. Using this relation the magnetic dipole interaction energy can be written [14, p. 4]

$$E_{M1}(J, J') = (-1)^{I+J'-F} \sqrt{(2J+1)(2I+1)} W(I, J'; I, J; F, 1)$$
$$\langle \Gamma_j J | |\mathbf{T}^{(1)}| |\Gamma_j J' \rangle \langle \Gamma_i I | |\mathbf{M}^{(1)}| |\Gamma_i I' \rangle$$

where $W(I, J'; I, J; F, 1)$ is a Racah W-coefficient. Now the F dependence may be factorized out and the interaction energy expressed in terms of the hyperfine interaction constant A as [14, p. 4]

$$A_J = \frac{\mu_I}{I} \frac{1}{\sqrt{J(J+1)}} \langle \Gamma_j J | |\mathbf{T}^{(1)}| |\Gamma_j J \rangle$$

$$A_{J,J-1} = \frac{\mu_I}{I} \frac{1}{\sqrt{J(2J-1)}} \langle \Gamma_j J | |\mathbf{T}^{(1)}| |\Gamma_j (J-1) \rangle .$$

Furthermore, the interaction energies are now

$$E_{\mathrm{M1}}(J, J) = \frac{1}{2} A_J C,$$

$$E_{\mathrm{M1}}(J, J-1) = \frac{1}{2} A_{J,J-1} [(K+1)(K-2F)(K-2I)(K-2J+1)]^{\frac{1}{2}},$$

where $C = F(F+1) - J(J+1) - I(I+1)$ and $K = I + J + F$.

If the wave function is approximated with an ASF expanded in jj-coupled CSFs as in equation (3.2), the diagonal and off-diagonal magnetic dipole hyperfine structure constants can be written [14, p. 4]

$$A_J = \frac{\mu_I}{I} \frac{1}{[J(J+1)]^{\frac{1}{2}}} \sum_{r,s} c_r c_s \langle \Gamma_r P J | |\mathbf{T}^{(1)}| |\Gamma_s P J \rangle$$

$$A_{J,J-1} = \frac{\mu_I}{I} \frac{1}{[J(2J-1)]^{\frac{1}{2}}} \sum_{r,s} c_r c_s \langle \Gamma_r P J | |\mathbf{T}^{(1)}| |\Gamma_s P(J-1) \rangle .$$

where the evaluation reduces to the calculation of matrix elements between CSFs. Angular recoupling may be set up to reduce the matrix element $\langle \Gamma_r P J | |\mathbf{T}^{(k)}| |\Gamma_s P J' \rangle$ to terms involving single-particle orbitals as [14, p. 4]

$$\langle \Gamma_r P J | |\mathbf{T}^{(k)}| |\Gamma_s P J' \rangle = \sum_{a,b} d_{ab}^k(rs) \langle n_a \kappa_a | |\mathbf{t}^{(k)}| |n_a \kappa_a \rangle .$$

The single-particle matrix elements can in turn be factorized into a reduced angular matrix element and a radial integral [14, p. 4]

$$\langle n_a \kappa_a | | \mathbf{t}^{(1)} | | n_b \kappa_b \rangle = -\alpha(\kappa_a + \kappa_b) \langle -\kappa_a | | \mathbf{C}^{(1)} | | \kappa_b \rangle [r^{-2}]_{n_a \kappa_a n_b \kappa_b},$$

where $n_a \kappa_a$ etc. are relativistic subshells and

$$[r^{-2}]_{n_a \kappa_a n_b \kappa_b} = \int_o^\infty r^{-2} \big[P_{n_a \kappa_a}(r) Q_{n_b \kappa_b}(r) + Q_{n_a \kappa_a}(r) P_{n_b \kappa_b} \big] dr.$$

4.2 Hyperfine Anomaly

In reality the nucleus has a finite extent, which will lead to a different value for the calculated hyperfine interaction constant when compared to the value calculated in the point nucleus approximation. The difference is known as the hyperfine anomaly, and is made up of two parts.

4.2.1 Breit-Rosenthal Effect

The first part is caused by the deviation of the nuclear charge distribution from the point charge approximation. A nuclear model with an extended charge distribution will lead to a different calculated A-value than one with a nuclear point charge model if electrons penetrate the extended nuclear volume. The difference is called the Breit-Rosenthal (BR) effect, and is parameterized by the Breit-Rosenthal correction ϵ_{BR} defined by the relation

$$A = A_p(1 + \epsilon_{BR}),$$

where A_p is the constant for a point nuclear model. s and $p_{1/2}$ electrons have non-zero probability densities at the location of the nucleus, and are therefore expected to be affected by the distribution of charge in the nucleus. Other electrons may also, due to electron-electron interactions, have a non-zero probability density at the nucleus [16, p. 2]. The BR-effect is often negligible, but can be significant for large Z ($\sim 20\%$ for $Z = 90$ [2, p. 12]).

4.2.2 Bohr-Weisskopf Effect

The deviation of the magnetic moment from a point dipole approximation may also affect the calculated value of A if electrons overlap with the distribution of magnetization. The result of this is the Bohr-Weisskopf (BW) effect parameterized by ϵ_{BW}, which gives the deviation in the magnetic dipole hyperfine interaction constant for an extended magnetisation nuclear model, compared to that of a point dipole nuclear model. The hyperfine structure constant is then

$$A = A_{p.d.}(1 + \epsilon_{BW}),$$

where $A_{p.d.}$ is the hyperfine structure constant for a nuclear model with a magnetic point dipole and a finite charge distribution. The effect is thus dependent on both electronic and nuclear properties, i.e. the electronic probability densities inside the nucleus and the distribution of nuclear magnetisation. This effect can be used to obtain information about the distribution of magnetisation in the nucleus [17, p. 4].

4.2.3 Differential Hyperfine Anomaly

Putting both the contributions together yields [16, p. 2]

$$A = A_p(1 + \epsilon_{BW})(1 + \epsilon_{BR}),$$

where A is the experimental value of the hfs constant. The electronic wave functions in complex atoms cannot be calculated with sufficient precision to determine ϵ_{BW} directly [17, p. 4]. It is however possible to determine the difference in ϵ_{BW} between two isotopes, the *differential* hyperfine anomaly [17, p. 4]. Taking the ratio between two isotopes cancels A_p and yields [16, p. 2]

$$\begin{aligned}
\frac{A_1}{A_2} &= \frac{g_I^{(1)}}{g_I^{(2)}} \frac{[1 + \epsilon_{BW}^{(1)}][1 + \epsilon_{BR}^{(1)}]}{[1 + \epsilon_{BW}^{(2)}][1 + \epsilon_{BR}^{(2)}]} \\
&\stackrel{\epsilon \ll 1}{\approx} \frac{g_I^{(1)}}{g_I^{(2)}}[1 + \epsilon_{BW}^{(1)} - \epsilon_{BW}^{(2)}][1 + \epsilon_{BR}^{(1)} - \epsilon_{BR}^{(2)}] \\
&\equiv \frac{g_I^{(1)}}{g_I^{(2)}}[1 +^1 \Delta_{BW}^2][1 +^1 \Delta_{BR}^2] \equiv \frac{g_I^{(1)}}{g_I^{(2)}}[1 +^1 \Delta^2],
\end{aligned}$$

where $^1\Delta^2$ is the differential hyperfine anomaly between isotope 1 and 2, divided into the BR- and BW-contributions $^1\Delta_{BR}^2$ and $^1\Delta_{BW}^2$, respectively.

Chapter 5

General Relativistic Atomic Structure Package 2018

The General Relativistic Atomic Structure Package 2018 (GRASP2018) [5] is a program package developed for performing calculations in relativistic atomic structure. It enables calculations of atomic properties such as energy levels, transition probabilities, oscillator strengths, lifetimes and hyperfine structure.

5.1   Defining the Nucleus

There are multiple models for the nuclear charge distribution used in atomic structure computations. The simplest is a point charge model, where the nuclear charge is concentrated at a single point at the center of the atom. This model is inaccurate for complex atomic systems, but is frequently used for simple systems, or as a starting point for more advanced calculations. Another model is the uniform distribution model which takes into account the finite size of the nucleus, which affects the behavior of the electronic system if electrons penetrate the nuclear volume. This is particularly relevant in heavy elements and high-energy experiments.

In GRASP2018 the nuclear charge distribution is modelled by a two-parameter Fermi distribution, which has a finite size and a smooth density profile. It is more advanced than the uniform distribution model in that it accounts for the nuclear charge distribution having a gradual transition from the central region to the surface, which gives a realistic description of the nuclear distribution [15, p. 5]. The Fermi charge density is given by

$$\rho(r) = \frac{\rho_f}{1 + e^{(r-c)/a}},$$

where c is the half-density radius such that $\rho(c) = \frac{1}{2}\rho(0)$ and a is the diffuseness parameter related to the skin thickness t by $t = a \cdot 4ln3$ [15, p. 5]. The skin thickness is the width over which the charge density drops from 90%

to 10% of the central value $\rho(0)$. These parameters may be experimentally determined, for example by fitting to scattering data, and they give the Fermi model a more flexible representation of the nuclear charge distribution than the uniform distribution model.

Experiments indicate a skin thickness of about $t = 2.3$ fm for most nuclei [15, p. 5], which is also the default value for all nuclei in GRASP2018. The program *rnucleus*, used to define the nuclear model, does however allow for revision of the root mean squared radius R, which alters the half-density radius c in the model, and the skin thickness t, which alters the diffuseness parameter a. It is also possible to edit the output file *isodata* directly, and alter either of the two Fermi parameters c and a directly.

The spherically symmetric charge distribution of the nucleus simplifies calculations of the electronic wave functions. If necessary, deformations of the nucleus can be accounted for by introducing an electric quadrupole moment, which describes the first-order polarization of the charge distribution. Higher-order multipole moments, such as the octupole moment, can also be used to characterize higher-order deformations.

In GRASP2018, the magnetic moment of the nucleus is modelled as a magnetic point dipole at the origin.

The nuclear properties necessarily input by the user are the atomic number Z, mass number A, spin I, dipole moment μ and quadrupole moment Q.

5.2   Generating the CSF basis for the ASF

The CSF basis is generated with the active set approach, described in the GRASP2018 manual [4, p. 40-41], where excitations from a reference state is done within a one-electron orbital basis. The reference is made up of important, strongly interacting CSFs (multireference), which includes the configurations of the targeted states, and may include other important configurations. The multireference contains only orbitals occupied by electrons, so-called spectroscopic orbitals, while the orbitals used for substitutions are called virtual orbitals. The latter are also referred to as correlation orbitals, as they are used to determine correlation between electron positions. CSFs describing electron correlation are created by substituting electron orbitals in the multireference with virtual orbitals corresponding to excited electrons. Equivalently, the orbital in the multireference is said to be excited to the virtual orbital. The spectroscopic orbitals are separated into core subshells and peel subshells, where core subshells are required to be fully occupied in all CSFs and the peel subshells may be allowed substitutions from virtual orbitals. The orbital set comprising the spectroscopic orbitals open for substitutions plus the virtual orbitals used as substitutions is called the active set.

A series of runs may be done where the active set is systematically increased, to achieve convergence of the expectation values. CSFs with single (S) and double (D) substitutions constitute the most important part of the ASF, while CSFs with triple (T) or more substitutions correspond to higher order correc-

tions since the DC Hamiltonian consists of one- and two-particle operators, resulting in Hamiltonian matrix elements of zero with the CSF generated by T or more substitutions.

The list of CSFs from which the ASF is constructed is created with the program *rcsfgenerate*. This program constructs all CSFs with the same parity and total angular momentum as the reference CSF, within a set of specified rules. These rules include which of the spectroscopic orbitals are active, meaning are allowed orbital replacements from virtual orbitals to form new CSFs, and the maximum number of orbital replacements allowed. Orbitals may also be set to minimum occupation such that all CSFs generated contain the minimum or more electrons in the given orbital.

Not all the generated CSFs interact, meaning have non-zero Hamiltonian matrix elements, with the CSFs in the multireference. These can without much loss of accuracy, be removed from the expansion [5, p. 42]. This removal is done with the program *rcsfinteract*.

5.3   Optimizing the Wave Function

Calculation of wave functions is a multi-step procedure. Given the CSF basis the ASF is optimized using first the MCDHF method and then (optionally) the RCI method. The first step is calculation of the spin-angular coefficients, done by the program *rangular*. The coefficients are stored in files read by the program *rmcdhf*, which carries out the scf procedure. Also taken as input are initial estimates of the radial orbitals, produced by the *rwfnestimate* program. This uses the nuclear model and the given CSFs to calculate the radial functions based on either the Thomas-Fermi (TF) approximation or screened hydrogenic (SH) functions. Converted non-relativistic Hartree-Fock radial orbitals or radial orbitals from a previous run may also be used. The final radial orbitals are obtained when the solution converges to some threshold, which is calculated as a weighted sum over changes in the radial orbitals. *rmcdhf* outputs the optimized radial functions and mixing coefficients. The file with the output radial functions, *rwfn.out*, is updated for each iteration such that if a run fails one can start over from the previous iteration by copying the output file to input with the command *cp rwfn.out rwfn.inp*. In the end the *rci* program may be run to adjust the mixing coefficients while keeping the orbital basis fixed, accounting for Breit and QED corrections. *rci* creates a restart file called *rci.res*, such that if a run fails one can restart from the point of failure by running *rci* with non-default settings.

5.4   Computing Observables

Once the ASF is optimized any observable can be calculated from it. For example, the *rhfs* program calculates the magnetic dipole and electric quadrupole hyperfine structure constants. Computations of the hyperfine structure con-
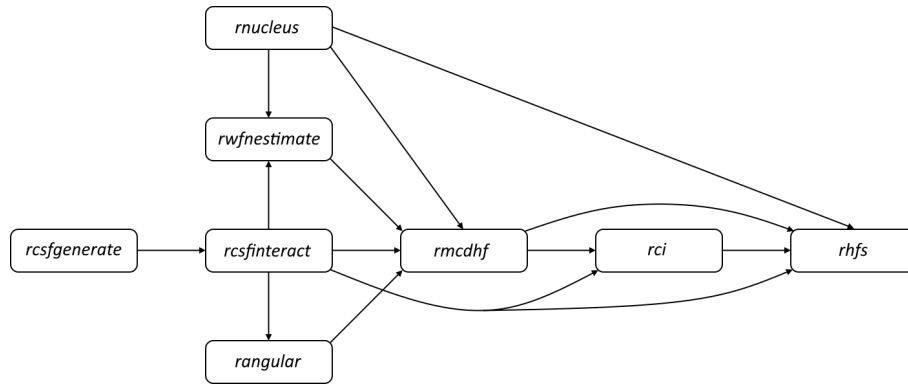
Figure 5.1: A typical sequence of programs, ending with a calculation of the hyperfine structure constant A. Arrows indicate that output files from one subprogram is taken as input by another.

stants are done in first order perturbation theory [13, p. 5], where the zero order wave functions are obtained with the Fermi distribution. The flowchart in figure 5.1 gives an overview of a typical sequence of programs, ending in a calculation of the hyperfine structure constant A.

Chapter 6

Computations on ^{207}Pb

6.1 Changing Parameters in GRASP2018

Certain parameters in GRASP2018 can be altered by the user. For example, the radial functions $P_{n\kappa}$ and $Q_{n\kappa}$ are defined on a grid [13, p. 4]

$$r_i = \frac{A}{Z}\left(e^{B(i-1)} - 1\right), i = 1, ..., \text{NNNP},$$

where as per the manual [4, p. 20-21], it is sometimes necessary to increase the number of grid points for neutral heavy to super heavy elements. This may be useful for hyperfine structure calculations, as more grid points close to the nucleus improves the resolution of electron/nucleus overlap. No recommended parameter values could be found for Pb, so the values recommended by Jönsson et al. [12, p. 3] for Hg were taken as a starting point. This meant the default number of grid points, 590 was changed to 2990, and the grid step size was changed to $H = 10^{-2}$. There was also a recommended value for the parameter RNT, which is further divided by Z, such that the recommended value for Hg, RNT $= 10^{-6}$, divided by $Z = 82$ for Pb yielded roughly the employed value RNT $= 1.2 \times 10^{-8}$. All the custom parameters are given in Table 6.1. The custom grid was used for most of the calculations, although some calculations were done with the default grid to test the necessity of utilizing the more computationally expensive custom grid for hyperfine anomaly calculations (section 7.4).

Parameter	Description	Default Value	Custom Value
NNNP	*maximum number of grid points*	590	2990
H	*grid step size*	2.0×10^{-2}	1.0×10^{-2}
RNT(^{207}Pb)	*1st non-zero grid point*	2.439×10^{-8}	1.2×10^{-8}

Table 6.1: Parameters changed in the GRASP2018 Package.

6.2 Nuclear Parameters

For computations on ^{207}Pb the default skin thickness and rms radius were used. These and other experimental values used to define the nuclear parameters are given in table 6.2. Moreover, figure 6.1 shows the normalized Fermi distribution $\rho(r)/\rho_f$ for the ^{207}Pb nuclear model as defined by these parameters.
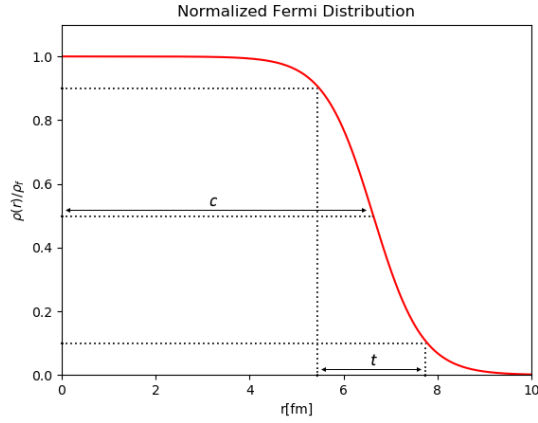
Figure 6.1: Fermi distribution with half-density radius c and skin thickness t for the nuclear model of ^{207}Pb.

Moreover, experimentally obtained values of the hyperfine structure constant for the states $6p^2\,{}^3P_1,{}^3P_2$ and $^1D_2$ and $6p7s\,{}^3P_1$ in ^{207}Pb are given in table 6.3.

Z	A	R	t	I	m	μ_I
		[fm]	[fm]	[$\hbar$]	[amu]	[μ_N]
82	207	5.4943(14) [1]	2.3 [15]	1/2 [18]	206.975896(13)[18]	0.5925839(9)[18]

Table 6.2: Experimental data used to define the nuclear model of ^{207}Pb. R is the rms charge radius, t is the skin thickness, I is the angular momentum and μ_I is the magnetic moment.

A($6p^2\,{}^3P_1$)	A($6p^2\,{}^3P_2$)	A($6p^2\,{}^1D_2$)	A($6p7s\,{}^3P_1$)
MHz	MHz	MHz	MHz
-2390.976(2)	2602.881(2)	609.818(8)	8802.0(1.6)

Table 6.3: Experimental values of the hyperfine structure constant for the states $6p^2\,{}^3P_1,{}^3P_2$ and $^1D_2$ and $6p7s\,{}^3P_1$ in ^{207}Pb, taken from Persson [17].

33

6.3   Obtaining Orbitals

Optimizing all radial orbitals together is desirable, but often not possible. Instead, an approach described in the GRASP2018 manual [4, p. 34] was used. Initially the spectroscopic orbitals were optimized and kept frozen in all further calculations. Virtual orbitals were then added and optimized in a layer by layer fashion, where each newly added layer was optimized while keeping the previous layers fixed.

The default threshold value of 1.56×10^{-8} for convergence in the scf procedure was used in all the computations.

6.3.1   Spectroscopic Orbitals

Computations were mostly done with the even parity $6p^2$ and odd parity $6p7s$ configurations together, although some single configuration calculations were also performed. When doing both configurations together and using the custom grid, all spectroscopic orbitals immediately achieved convergence together. However, slight convergence problems were encountered when using the default grid. More serious convergence problems occurred in the single-configuration calculations, especially for the $6p7s\,^3P_1$ state.

When the spectroscopic orbitals did not achieve convergence together, several techniques described in the manual [4, c. 13] were employed. First starting with the inner core and gradually building the core orbitals was attempted. This is the preferred method for converging the spectroscopic orbitals [4, p. 271], and was mostly successful, except for the $6s$ and $7s$ orbitals. Even with the other spectroscopic orbitals optimized together, these still did not converge when varied alone. Therefore, the additional technique of increasing the nuclear charge [4, p. 284] was used. The already optimized orbitals were kept fixed as $6s$ and $7s$ were optimized for $Z = 82.5$, and then in multiple runs as the charge was gradually reduced back to $Z = 82$. Thereafter, all spectroscopic orbitals achieved convergence together.

6.3.2   Correlation Orbitals

The virtual orbitals were introduced in a layer by layer fashion as described in the manual [4, p. 33-34]. Here a virtual layer means a set of orbitals where the angular quantum number κ is different for every orbital. The orbitals included in each layer are given in table 6.5. After convergence of the spectroscopic orbitals, each virtual layer was introduced in turn and all orbitals in the each layer optimized together. The previously optimized layers were then kept fixed, while the next layer was introduced and optimized. Up to five (usually four) virtual layers were included in the calculations. The TF approximation was used to give initial estimates of the radial orbitals when possible. Screened hydrogenic functions were used only for the $5f$ orbital, since the program failed to generate a TF function for this orbital.

The CSF expansions were generated with the *rcsfgenerate* program. Removal of non-interacting CSFs using *rcsfinteract* was done for all expansions generated with S and SD substitutions. However, reduction was not done for expansions generated by allowing SDT substitutions, since all CSFs corresponding to T excitations are then removed. This is because the DC Hamiltonian is a sum over one- and two particle operators, and as such all CSFs resulting from more than two orbital replacements will have Hamiltonian matrix elements of zero with the CSF it was generated from. Therefore, reduction with *rcsfinteract* removes all CSFs corresponding to T excitations.

After optimization of each virtual layer, the RCI procedure was done where the transverse photon interaction, vacuum polarization and self energy corrections were included in the calculations. The program calculates the transverse photon interaction in the low frequency limit by multiplying with a scale factor, which was set to 10^{-6}, a commonly applied value [5, p. 35]. Self energy corrections were included for all orbitals with principal quantum number $n \leq 6$.

6.4 Single Substitutions

CSFs resulting from S substitutions may be classified as either valence (v) correlation or core (c) correlation based on whether the substitution was made from a valence orbital or a core orbital. S substitutions from a core subshell correspond to polarization of the core caused by the electrostatic interaction with valence electrons [7, p. 171]. In the CF approximation closed subshells in the inner core contribute zero to the hfs, since they have a spherically symmetric charge distribution and thus create net zero electric and magnetic field at the nucleus [7, p. 171]. Also closed s-subshells make zero contribution, because the two electrons have equal spin densities with opposite directions ($m_s = \pm\frac{1}{2}$). However, the closed subshells can stongly affect the hyperfine structure when polarized through Coulomb interaction with open subshells [7, p. 171]. The exchange contribution to the interaction is attractive for core- and valence electrons with the same spin orientation, which reduces the repulsion and pulls the core electron towards the valence subshell. Polarization of s-subshells is particularly important, because when the two s-electrons have different spin densities in the nuclear volume, a contact interaction is induced. Here a tiny distortion can cause a major effect due to the high densities of inner s-electrons at the nucleus [7, p. 171].

Since the hyperfine interaction is described by one-particle operators, only CSFs corresponding to S substitutions need to be included in the ASF expansion to first approximation [7, p. 171]. Therefore, the calculations based on S substitutions were expected to capture the bulk of the hyperfine structure. S substitutions were allowed to four layers of virtual orbitals, from all subshells of the s- and p-symmetries excluding $1s$. In the initial run, substitutions were allowed from the valence subshells $7s$, $6p$ and $6s$, before the core subshells were introduced in subsequent runs, in the order $5p$, $5s$,...,$2p$, $2s$. For each new set of active peel subshells calculations were done to one,...,four virtual layers. After

optimization of each virtual layer, the RCI was done and the hyperfine structure constants calculated. The results are presented in figure 6.2. The final configuration was used as the basis for a calculation of the BR-effect (chapter 7).
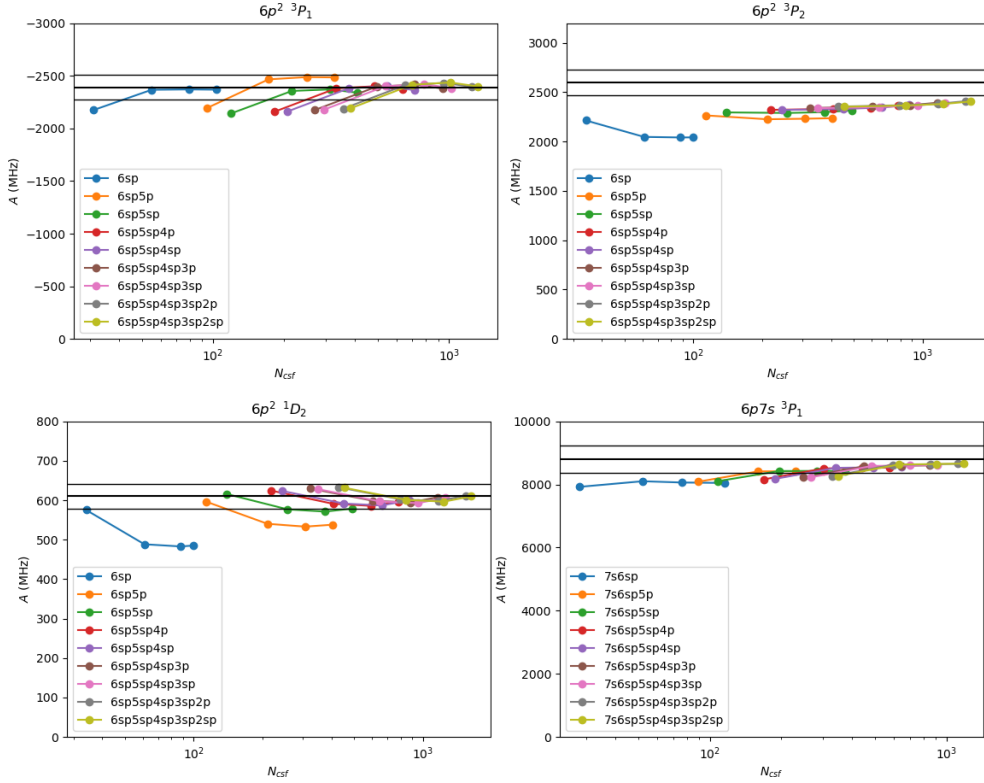
Figure 6.2: Unrestricted S substitutions allowed. Each data series correspond to one set of active peel subshells and the four data points in each series correspond to the $1st, ..., 4th$ virtual layer. The horizontal black lines in each graph indicate the experimental value of A for the given state, and error bars of $\pm 5\%$.

The runs based on S substitutions achieved convergence toward the experimental A-value for all states, as the active set was increased. In the end the results were excellent in $6p^{2\,3}P_1$ and $6p^{2\,1}D_2$, good in $6p7s^{3}P_1$ and somewhat off in $6p^{2\,3}P_2$. This indicates that correlation beyond the first approximation represented by S substitutions is more important in the latter state. For all four states the final expansion, generated by allowing S excitations from $7s6sp5sp4sp3sp2sp$ to four virtual layers gave the most accurate calculated A-value. The deviation from the experimental value of A for all states is given in table 6.4.

Moreover, table 6.5 shows the orbitals included in each virtual layer, plus the change in the calculated value of A after introduction of each virtual layer

State	$6p^2\,^3P_1$	$6p^2\,^3P_2$	$6p^2\,^1D_2$	$6p7s\,^3P_1$
$\delta A/A_{\mathrm{exp}}[\%]$	0.306	-7.52	-0.00889	-1.61

Table 6.4: Error in A for the expansion generated by S excitations from $7s6sp5sp4sp3sp2sp$ to four virtual layers, compared to the experimentally measured value A_{exp}. Here $\delta A/A_{\mathrm{exp}} \equiv (A_{\mathrm{calc}} - A_{\mathrm{exp}})/A_{\mathrm{exp}}$.

with the maximum set of active peel subshells.

Virtual layer	Orbitals	$\delta A/A[\%]$ $6p^2\,^3P_1$	$\delta A/A[\%]$ $6p^2\,^3P_2$	$\delta A/A[\%]$ $6p^2\,^1D_2$	$\delta A/A[\%]$ $6p7s\,^3P_1$
1st	8s 7p 6d 5f	34.34	-16.36	-47.38	8.247
2nd	9s 8p 7d 6f	10.24	0.5616	-4.878	4.351
3rd	10s 9p 8d 7f	0.8598	0.6399	-0.7323	0.1965
4th	11s 10p 9d 8f	-1.548	1.070	2.239	0.1512

Table 6.5: Orbitals included in the different virtual layers. Changes calculated relative to the value obtained at the previous layer, with S-substitutions from $7s6sp5sp4sp3sp2sp$.

6.5 Double Substitutions

The correlation effects represented by CSFs generated from D substitutions are categorized in a few ways. Valence-valence (vv) correlation means that both substitutions are made from valence orbitals. The valence orbitals have the least energy difference from the virtual orbitals, and are therefore expected to contribute significantly to the improvement of the wave function. Core-core (cc) correlation means that both substitutions are made from a core orbital. These account for interactions between electrons in the tightly bound core, which is particularly important in heavy atoms with many electrons, where the core electrons are tightly packed. Core-valence (cv) correlation means that one substitution is made from a core orbital and one from a valence orbital. These CSFs represent polarization of the electron core caused by the valence electrons. Deep core-valence correlation is important for calculations of hyperfine structure [4, p. 42].

The first CSF expansions were generated with all v and vv substitutions from the $7s$, $6p$ and $6s$ valence orbitals to one,..., four layers of virtual orbitals. Thereafter, one core subshell at the time was opened for c, cv and cc substitutions, in the sequence $5p$, $5s$,...,$3p$. The RCI was performed and the hyperfine structure constants calculated after optimization of each virtual layer. The development of the calculated A values as the active set increases is given in figure 6.3. The figure also shows a single series based on SDT substitutions.

The calculations based on unrestricted SD substitutions lead to convergence towards the experimental value and yielded quite good results in all states except

Virtual layer	Orbitals	$\delta A/A[\%]$ $6p^2\,^3P_1$	$\delta A/A[\%]$ $6p^2\,^3P_2$	$\delta A/A[\%]$ $6p^2\,^1D_2$	$\delta A/A[\%]$ $6p7s\,^3P_1$
1st	*8s 7p 6d 5f*	-42.4916	-8.5830	-14.0986	7.8321
2nd	*9s 8p 7d 6f*	-0.1156	-2.5155	-18.9882	3.2410
3rd	*10s 9p 8d 7f*	-6.2586	-3.8912	-13.7835	1.3193
4th	*11s 10p 9d 8f*	1.8021	2.7840	4.1572	-1.1938

Table 6.6: Orbitals included in the different virtual layers. Changes calculated relative to the value obtained at the previous layer, with SD-excitations from $7s6sp5sp4sp$.

$6p^2\,^1D_2$. The error between the experimental and calculated values of A using the biggest expansion is given in table 6.7.

State	$6p^2\,^3P_1$	$6p^2\,^3P_2$	$6p^2\,^1D_2$	$6p7s\,^3P_1$
$\delta A/A_{\exp}[\%]$	3.97	-2.65	29.5	-2.23

Table 6.7: Error in A for the expansion generated by unrestricted SD excitations from $7s6sp5sp4sp3p$ to four virtual layers, compared to the experimentally measured value $A_{\exp}$. Here $\delta A/A_{\exp} \equiv (A_{\mathrm{calc}} - A_{\exp})/A_{\exp}$.

In $6p^2\,^1D_2$ it was clear that SD excitations from core subshells causes an overestimation of the hyperfine structure which was not caused by S substitutions alone, meaning it is an effect of cv and/or cc correlation. The tendency is present already from activation of $5s$, but here it manages to recover by the *4th* virtual layer. It is possible that further virtual layers would have caused a convergence towards the experimental also with additional peel subshells active. It is not known why the problem arises, but it is believed to not be due to lacking correlation involving peel subshells of the d- and f-symmetries. Runs were attempted (not presented) where $5d$, $4f$, $4d$ and $3d$ were activated, which made the problem worse and also lessened results in other states.

That the effect decreases with activation of higher virtual layers may indicate that it is an effect of energy similarity between the core subshell and the virtual subshell to which the excitation is made. The extent of mixing between different configurations depends on their energy differences. Near-degeneracy effects occur when two orbitals have similar energies, leading to strong electron-electron interactions. The cv correlation may then cause the valence subshell to contract excessively which overestimates the hyperfine structure.

In terms of accuracy, only in $6p^2\,^3P_2$ did the calculations based on SD substitutions outdo the calculations based on S substitutions, strenghtening the belief that vv and cv correlation were of importance in this state. The poorer results in the other states is believed to be because with only S substitutions, correlation deeper in the electron core was considered.

6.6 Triple Substitutions

For the calculations based on allowing unrestricted SDT substitutions, only the valence $7s$, $6p$ and $6s$ orbitals were kept active because the number of CSFs in the expansion increases very rapidly when T substitutions are allowed. Thus, it was deemed not feasible to active core subshells in this case. Therefore, all CSFs in the expansions corresponded to replacements of three valence orbitals with virtual orbitals, which may be classified as valence-valence-valence (vvv) correlation. The $7s$, $6p$ and $6s$ orbitals were kept active and substitutions allowed to one,...,five virtual layers. Here the extra ($5th$) virtual layer $\{12s, 11p, 10d, 8f\}$, not used in any other calculation, was added. After optimization of each virtual layer, the RCI was performed and the hyperfine structure constants calculated. The results are included as a single series in figure 6.3.

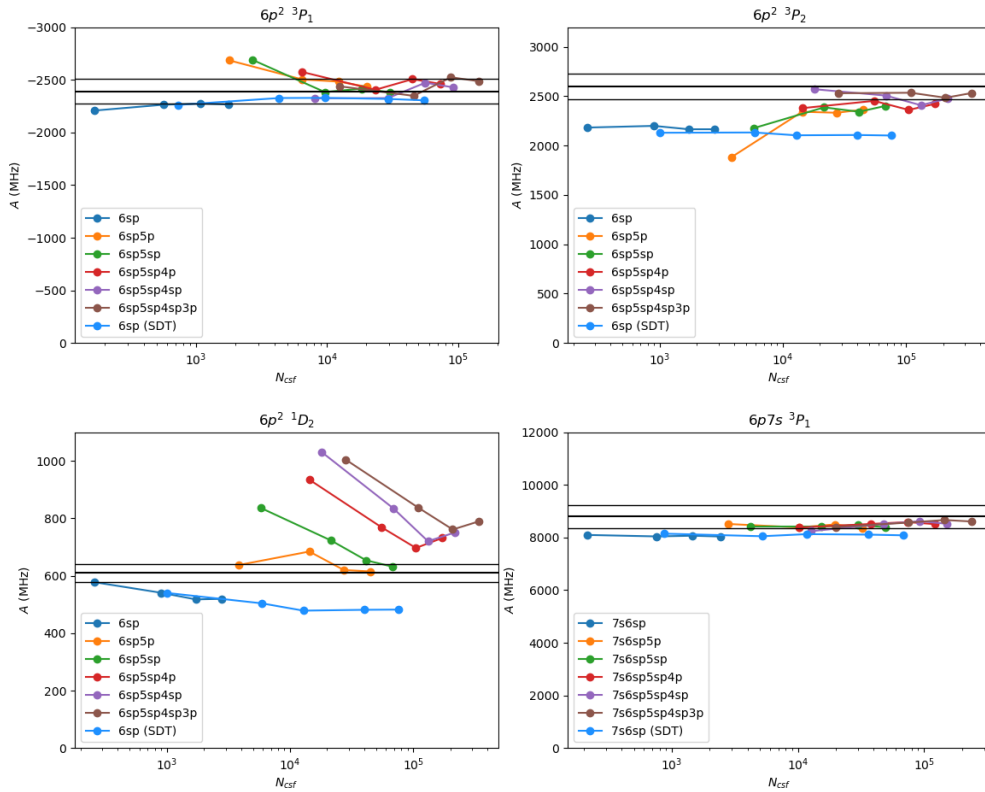Figure 6.3: Unrestricted SD substitutions allowed, except one series with unrestricted SDT substitutions. Each data series correspond to one set of active peel subshells and the four(five) data points in each series correspond to the $1st, ..., 4th(5th)$ virtual layer. The horizontal black lines in each graph indicate the experimental value of A for the given state, and error bars of $\pm 5\%$.

39

It is clear that accounting for vvv correlation did not alter the calculated A values a lot, when compared to the calculations involving only vv correlation. This is in agreement with expectations based on theory, as CSFs generated by T substitutions correspond to higher order corrections. Overall, the calculations based on SDT substitutions gave quite poor results, indicating that all core polarization should not be neglected. Figure 6.8 shows the error between the calculated A-values for the expansion generated by SDT excitations from $7s6sp$ to five virtual layers, relative to the experimental value.

State	$6p^2\,{}^3P_1$	$6p^2\,{}^3P_2$	$6p^2\,{}^1D_2$	$6p7s\,{}^3P_1$
$\delta A/A_{\mathrm{exp}}[\%]$	-3.59	-19.2	-20.9	-8.18

Table 6.8: Error in A for the expansion generated by SDT excitations from $7s6sp$ to five virtual layers, compared to the experimentally measured value A_{exp}. Here $\delta A/A_{\mathrm{exp}} \equiv (A_{\mathrm{calc}} - A_{\mathrm{exp}})/A_{\mathrm{exp}}$.

6.7 Optimizing Performance

Computations were done on the authors PC and on the Idun cluster [19], using both serial and mpi versions of the GRASP2018 software. With parallel computing it was possible to run on anywhere between one and 18 cores at one time. It was found that read speed bottlenecks often slowed the run-time such that adding more cores actually decreased performance. This was especially bad in the *rmcdhf* program where it was found that for the default grid four cores yielded the best performance in many cases. The custom grid appeared to make the read-bottlenecks even worse to the point where the serial version of *rmcdhf* was the quickest. These issues were not as significant in the *rci* program where typically four to 10 cores were used. The *rangular* program had no issues with read-bottlenecks, but was nevertheless limited in that it needs to run on the same number of cores as *rmcdhf*. Fortunately, the spin-angular coefficients are independent of the nuclear rms radius R and skin thickness t, such that *rangular* must only be ran once for each CSF expansion when doing calculation of the BR-effect (chapter 7).

Chapter 7

Parametric Study of the Breit-Rosenthal Effect in Pb I

7.1 Variation in Radius

Experimental values of the rms radii $R(A)$ of lead isotopes were taken from Angeli and Marinova [1], who lists values for all isotopes with $A = 182, ..., 214$. Beyond this an extrapolation was done to cover the entire isotope range $A = 178, ..., 220$. The obtained range for $R(A)$ corresponded to a range of deviation in the mean squared radius $\langle r_n^2 \rangle$ from the ^{207}Pb reference isotope of between $-1.466(\text{fm})^2$ and $+0.779(\text{fm})^2$, as calculated with the relation [1, p. 2]

$$R^2(A) = R^2(A') + \delta \left\langle r_n^2 \right\rangle^{A'A} .$$

This range was divided into 10 roughly equally spaced points for which the hfs constant was calculated. For each calculation, all orbitals were optimized through MCDHF calculations using the new nuclear parameters. Initial estimates of radial orbitals were given by TF functions at every step. After optimization of each virtual layer, the RCI was done and the hfs constant calculated. The obtained A for every value of $\delta \left\langle r_n^2 \right\rangle$ was compared to the value A_0 calculated with the reference parameters. With the obtained values of $\delta A/A_0$, the BR effect was approximated by the proportionality constant λ in the linear fit $\lambda \langle r_n^2 \rangle$.

Such a parametric study of the BR effect was carried out for multiple CSF expansions. These expansions were generated with the following rules:

1. Unrestricted SD excitations allowed from $7s6sp$.

2. Unrestricted SDT excitations allowed from $7s6sp$.

3. Unrestricted SD excitations allowed from $7s6sp5sp$.

4. Unrestricted SD excitations allowed from $7s6sp5sp4sp$.

5. Unrestricted S excitations allowed from $7s6sp5sp4sp3sp2sp$.

For each of these sets of active peel subshells four CSF expansions were created, allowing substitutions to one, two, three and four virtual layers, respectively. This yielded a total of 20 CSF expansions for which the proportionality constant λ in the linear fit $\lambda\langle r_n^2\rangle$ for the BR effect was calculated in the manner outlined. For all expansions, λ was obtained simultaneously for all states. This was done using linear regression with a no-intercept model, forcing the fit through the origin. In this model, λ was calculated as

$$\lambda = \frac{\sum_i \langle r_n^2\rangle_i \left(\frac{\delta A}{A_0}\right)_i}{\sum_i \langle r_n^2\rangle_i^2},$$

where the sum is over the values corresponding to the 10 sets of nuclear parameters. The corresponding coefficients of correlation are

$$R_0^2 = \lambda^2 \frac{\sum_i \langle r_n^2\rangle_i^2}{\sum_i \left(\frac{\delta A}{A_0}\right)_i^2}.$$

These coefficients indicate how effectively the data points are approximated by the linear fit, taking values between 0 and 1, where closer to 1 means better approximation. The coefficients of correlation can thus be interpreted as indicating how well the BR effect is represented by $\lambda\langle r_n^2\rangle$.

As an example, the data for the expansion created by allowing SD substitutions from the $7s6sp5sp$ subshells to four virtual layers is given in table 7.1. The same data is represented graphically in figure 7.1, along side the calculated linear fit for each state.

Furthermore, the proportionality constant λ in the linear fit $\lambda\langle r_n^2\rangle$ for the BR effect, as calculated with all 20 expansions, are shown graphically in figure 7.2. This demonstrates how the calculated proportionality constants develop as the active set is increased. In addition, the value of λ calculated with only the multireference CSFs is shown. All calculations were done with the extended grid. For all the obtained λ-values, the corresponding coefficient of correlation was $R_0^2 > 0.99$ with a single exception being that the calculation based on SDT excitations from $7s6sp$ to four virtual layers having $R_0^2 \approx 0.84$. All data is given in the Appendix.

$\delta \langle r_n^2 \rangle$ [fm^2]	R [fm]	$\delta A/A_0[\%]$ $6p^2 \, ^3P_1$	$\delta A/A_0[\%]$ $6p^2 \, ^3P_2$	$\delta A/A_0[\%]$ $6p^2 \, ^1D_2$	$\delta A/A_0[\%]$ $6p7s \, ^3P_1$
-1.466	5.3592	0.1234	0.008871	-0.1261	0.09691
-1.224	5.3817	0.1028	0.007371	-0.1051	0.08070
-0.981	5.4043	0.08209	0.005884	-0.08390	0.06445
-0.738	5.4268	0.06151	0.004398	-0.06288	0.04829
-0.493	5.4493	0.04098	0.002935	-0.04189	0.03217
-0.247	5.4718	0.02047	0.001465	-0.02093	0.01607
0	5.4943	0	0	0	0
0.259	5.5178	-0.02135	-0.001527	0.02183	-0.01676
0.518	5.5413	-0.04267	-0.003050	0.04362	-0.03348
0.779	5.5648	-0.06395	-0.004568	0.06539	-0.05019

Table 7.1: Relative change in the hfs constant $\delta A/A_0$ under variation in the mean squared radius $\langle r_n^2 \rangle$ wrt the reference nucleus ^{207}Pb, calculated with the expansion created by allowing SD substitutions from the $7s6sp5sp$ subshells to four virtual layers.

7.2 Variation in Skin Thickness

Varying the nuclear skin thickness t, and consequently the diffuseness parameter a, alters the shape and slope of the charge distribution near the surface of the nucleus. This corresponds to varying the higher order radial moments of the nuclear charge distribution, beyond the rms radius R. Such calculations give an indication of how much of the BR effect results from higher order radial moments, and whether the linear fit is valid for the different isotopes. In order to maintain R when varying the skin thickness, the half-density radius c is also altered to offset the change.

Calculations varying the skin thickness were done jointly for all states, using the extended grid. The expansion based on S excitations from $7s6sp5sp4sp3sp2sp$ to four virtual layers was used, and the nuclear skin thickness was varied by ± 0.1fm and ± 0.2fm from the default value 2.3fm. These deviations correspond to one and two standard deviations in the skin thickness obtained for atoms with nucleon number $A > 16$ by fitting to scattering data [3, p. 31-36].

Figure 7.3 shows the relative change in the calculated hfs constant A for all states, as the skin thickness is varied while keeping the rms radius constant at $R = 5.4943$fm. Similarly to the proportionality constant λ for variation in radius, the proportionality constant τ in the linear fit $\tau \delta t$ is introduced for the skin thickness. The linear fit is done with the same no-intercept model as for λ. In units of %fm^{-1}, the values $\tau(6p^2 \, ^3P_1) = 0.0351$, $\tau(6p^2 \, ^3P_2) = 0.00327$, $\tau(6p^2 \, ^1D_2) = -0.0375$ and $\tau(6p7s \, ^3P_1) = 0.0278$ were obtained. The corresponding coefficients of correlation were all > 0.998.

Moreover, for each of the given t-values, a full calculation of the BR effect, as represented by the linear fit $\lambda \langle r_n^2 \rangle$, was done in the manner described in section 7.1. The values of λ obtained for the different skin thicknesses and the
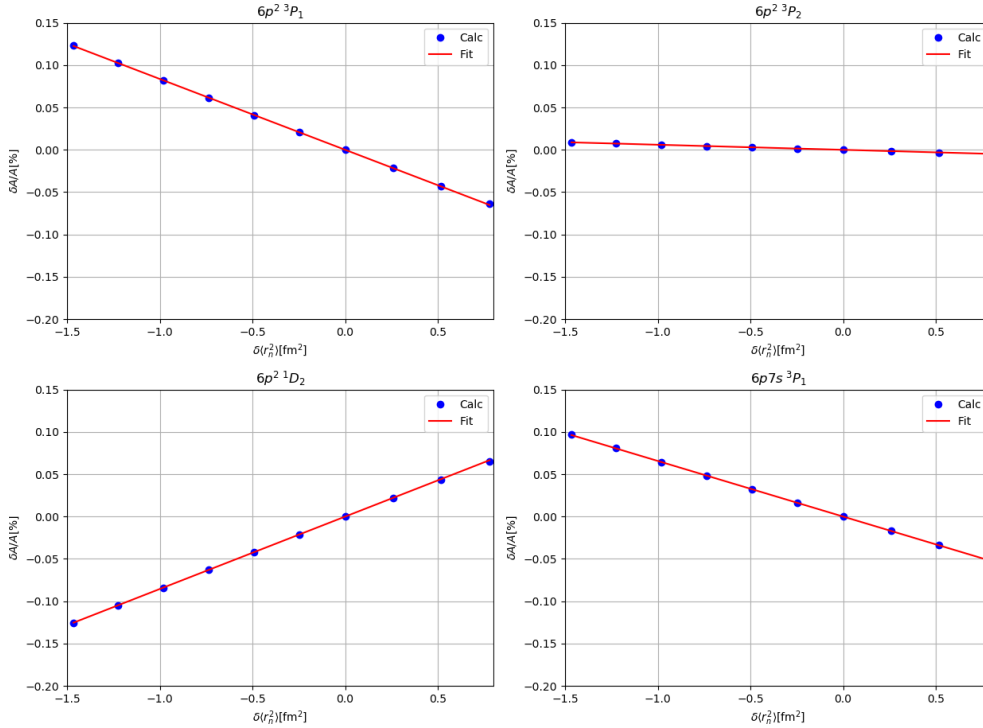
Figure 7.1: Relative change in the hfs constant $\delta A/A_0$ against deviation in the mean squared radius of the nuclear Fermi charge distribution $\delta \langle r_n^2 \rangle$ from the reference nucleus with hfs constant A_0. Based on the expansion generated with SD excitations from the $7s6sp5sp$ subshells to four virtual layers. The red line represents the linear fit $\lambda \delta \langle r_n^2 \rangle$.

corresponding deviations from the reference model with $t = 2.3$fm are presented in table 7.2.

7.3 Even and Odd Parity

There was some worry that doing calculations with both the even parity $6p^2$ and odd parity $6p7s$ configurations at the same time would lead to error. Therefore, some calculations were done both with the even parity states alone, and even and odd parity states together to compare results. These calculations were based on SD excitations from $6sp$ and $6sp5sp$ to one,...,four virtual layers. The difference in the calculated λ-values for the states in the $6p^2$ configuration are given in table 7.3.
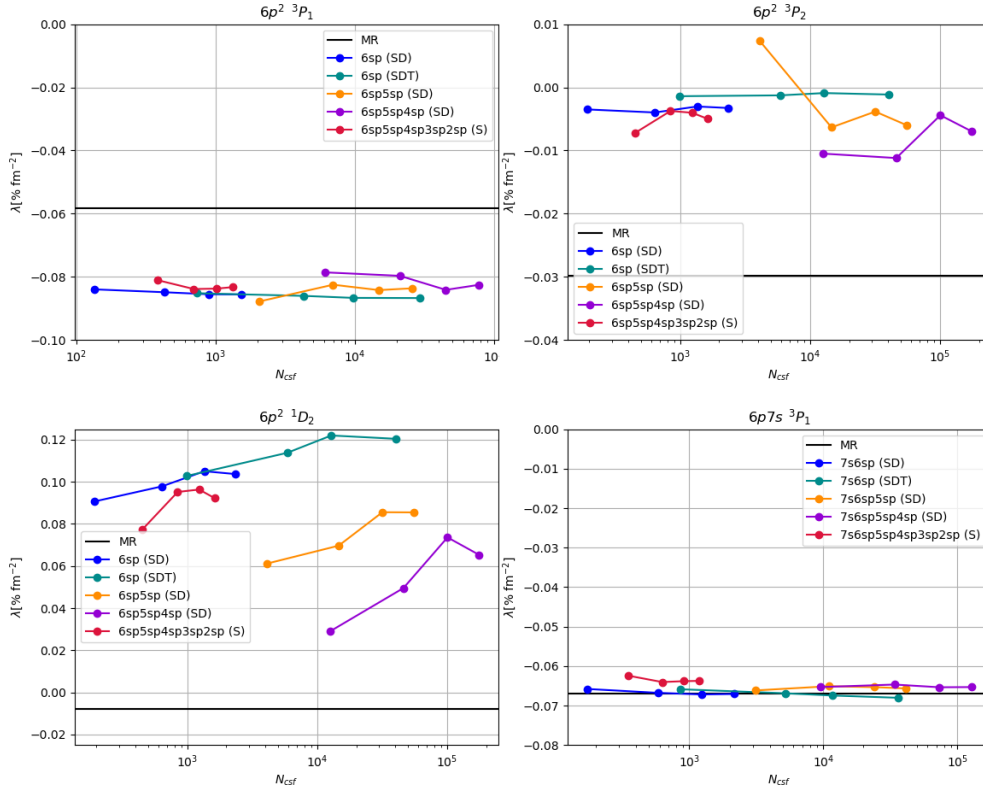
Figure 7.2: The proportionality constant λ in the linear fit $\lambda\langle r_n^2\rangle$ for the BR effect. Each data series correspond to one set of active peel subshells and the four data points in each series correspond to one,...,four virtual layers. The horisontal black line in each plot indicates the value of λ calculated with only the multireference CSFs.

7.4   Default Grid

The extended grid recommended for heavy elements led to significantly increased demand for computational resources. It was therefore decided to run a computation with the default grid and compare results to a corresponding computation done with the extended grid, in order to assess the necessity of using the computationally expensive extended grid in hyperfine anomaly calculations. Single configuration calculations for $6p^2$ allowing SD excitations from the $6sp5sp$-subshells to one,...,four virtual layers were done with both the default and the extended grid. The proportionality constant λ in the linear fit $\lambda\langle r_n^2\rangle$ for the BR effect was calculated for each of the virtual layers and results compared. The results are given in table 7.4. The corresponding coefficients of correlation were all > 0.986, and often > 0.999.
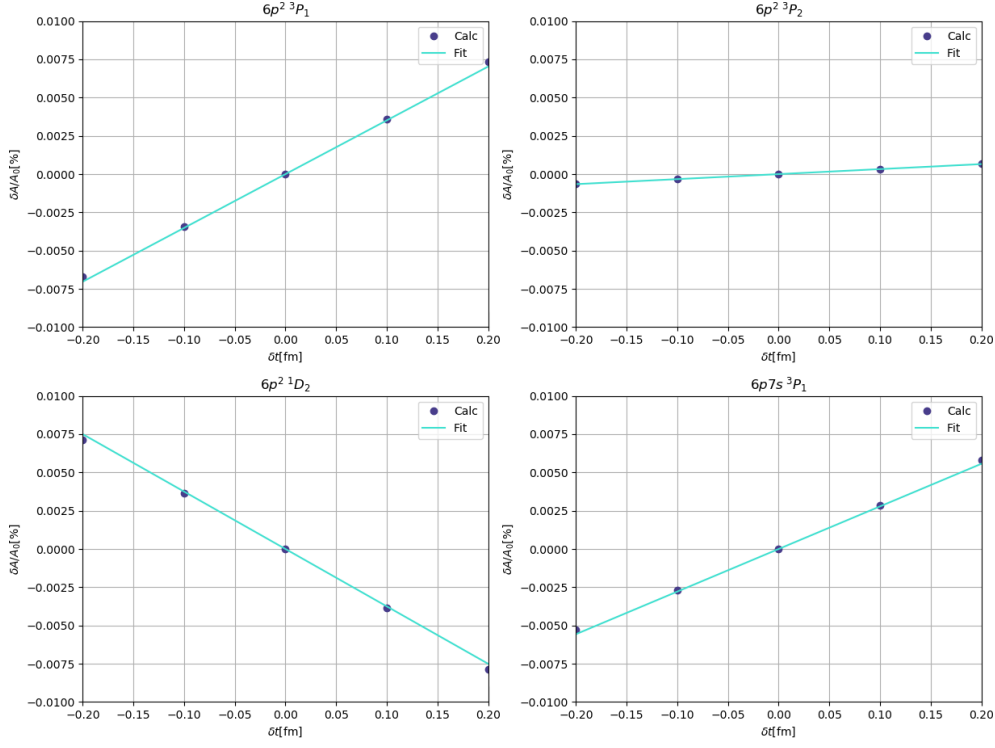
Figure 7.3: Relative change in the hfs constant $\delta A/A_0$ against variation δt in the skin thickness of the nuclear Fermi charge distribution from the reference nucleus with hfs constant A_0, based on the expansion generated with S excitations from $7s6sp5sp4sp3sp2sp$ to four virtual layers. The straight line is the linear fit $\tau\delta t$.

	$6p^2\,{}^3P_1$		$6p^2\,{}^3P_2$		$6p^2\,{}^1D_2$		$6p7s\,{}^3P_1$	
δt	λ	$\delta\lambda/\lambda_0$	λ	$\delta\lambda/\lambda_0$	λ	$\delta\lambda/\lambda_0$	λ	$\delta\lambda/\lambda_0$
[fm]	[% fm^{-2}]	[%]	[% fm^{-2}]	[%]	[% fm^{-2}]	[%]	[% fm^{-2}]	[%]
-0.2	-0.08295	-0.3692	-0.005156	3.600	0.09174	-0.5547	-0.06368	-0.1174
-0.1	-0.08317	-0.1013	-0.004969	-0.1632	0.09216	-0.1049	-0.06368	-0.1073
0	-0.08326	0	-0.004977	0	0.09225	0	-0.06375	0
0.1	-0.08335	0.1072	-0.004985	0.1686	0.09235	0.1109	-0.06382	0.1124
0.2	-0.08344	0.2203	-0.004994	0.3434	0.09246	0.2280	-0.06390	0.2300

Table 7.2: The proportionality constant λ in the linear fit $\lambda\langle r_n^2\rangle$ for the BR effect, calculated for deviations in skin thickness δt from the reference model ($t = 2.3$fm).

7.5 Discussion

7.5.1 Variation in Radius

The proportionality constant λ in the linear fit $\lambda\langle r_n^2\rangle$ for the BR effect was calculated for 20 CSF expansions of various sizes. For the $6p^2\,{}^3P_1$ and $6p7s\,{}^3P_1$ states,

SD substitutions from $6sp$				
State	$\Delta\lambda^{(1)}[\%]$	$\Delta\lambda^{(2)}[\%]$	$\Delta\lambda^{(3)}[\%]$	$\Delta\lambda^{(4)}[\%]$
$6p^2\,^3P_1$	-0.631283	-0.688693	-0.769825	-0.343677
$6p^2\,^3P_2$	7.73631	14.83573	32.2143	4.04054
$6p^2\,^1D_2$	-9.31160	-4.63566	-6.17307	-2.44642
SD substitutions from $6sp5sp$				
State	$\Delta\lambda^{(1)}[\%]$	$\Delta\lambda^{(2)}[\%]$	$\Delta\lambda^{(3)}[\%]$	$\Delta\lambda^{(4)}[\%]$
$6p^2\,^3P_1$	0.614040	0.629629	-0.289138	0.149315
$6p^2\,^3P_2$	-436.589	-2.33977	5.42864	1.78836
$6p^2\,^1D_2$	9.65980	-10.3772	-10.9288	-4.91634

Table 7.3: Differences in the calculated proportionality constant λ in the linear fit $\lambda\langle r_n^2\rangle$ for the BR effect for a multiconfiguration calculation with both $6p^2$ and $6p7s$, compared to a single configuration calculation with $6p^2$. Here $\Delta\lambda \equiv [\lambda(\text{Multi}) - \lambda(\text{Single})]/\lambda(\text{Single})$, and $\lambda^{(N)}$ is the value calculated for the expansion based on allowing excitations to N virtual layers.

State	$\lambda^{(1)}[\%\,\text{fm}^{-2}]$	$\lambda^{(2)}[\%\,\text{fm}^{-2}]$	$\lambda^{(3)}[\%\,\text{fm}^{-2}]$	$\lambda^{(4)}[\%\,\text{fm}^{-2}]$
Extended Grid				
$6p^2\,^3P_1$	-0.08728	-0.08198	-0.08446	-0.08325
$6p^2\,^3P_2$	-0.002192	-0.006498	-0.003730	-0.005965
$6p^2\,^1D_2$	0.05575	0.07774	0.09603	0.09028
Default Grid				
$6p^2\,^3P_1$	-0.08728	-0.08198	-0.08445	-0.08351
$6p^2\,^3P_2$	-0.002196	-0.006493	-0.003641	-0.005892
$6p^2\,^1D_2$	0.05574	0.07774	0.09606	0.08991
Difference in λ (extended to default grid)				
	$\delta\lambda^{(1)}[\%]$	$\delta\lambda^{(2)}[\%]$	$\delta\lambda^{(3)}[\%]$	$\delta\lambda^{(4)}[\%]$
$6p^2\,^3P_1$	-0.007206	0.005355	-0.01131	0.3219
$6p^2\,^3P_2$	0.1948	-0.08572	-2.384	-1.218
$6p^2\,^1D_2$	-0.01643	0.004760	0.03460	-0.4029

Table 7.4: The proportionality constant λ in the linear fit $\lambda\langle r_n^2\rangle$ for the BR effect, calculated with the default and extended grid, and the difference $\delta\lambda$ between the grids. Based on the expansions generated by allowing SD excitations from $6sp5sp$ to one,...,four virtual layers.

the 20 obtained values of λ in units of $\%\text{fm}^{-2}$ were all $\in (-0.08781, -0.07859)$, and $\in (-0.07231, -0.06242)$ respectively, with no two values having relative difference of more than $\approx 11\%$ and $\approx 16\%$, respectively. Including only the values calculated at the $4th$ virtual layer in each series, these intervals are reduced to $(-0.08672, -0.08252)$ and $(-0.06803, -0.06375)$ with no relative error of greater than $\approx 5\%$ and $\approx 7\%$, respectively. This is considered justified since all corresponding series of A-calculations in the ^{207}Pb reference isotope achieved con-

vergence towards the experimental value at the $4th$ virtual layer in both $6p2\,^3P_1$ and $6p7s\,^3P_1$. Moreover, in both states the expansions including only v, vv and vvv correlation yielded λ-values stacked at the lower end of the latter intervals, while the expansions adding c, cv and cc correlation yielded values towards the upper. Since the latter expansions more accurately reproduced the experimental value of A in the ^{207}Pb reference isotope, it was decided to recommend values slightly toward the higher end of the intervals as the correct λ-values. Specifically, $\lambda(6p2\,^3P_1) = -0.083(2)\%\mathrm{fm}^{-2}$ and $\lambda(6p7s\,^3P_1) = -0.065(3)\%\mathrm{fm}^{-2}$ are recommended. The uncertainties are chosen to extend more than twice the range of the aforementioned λ-values.

Furthermore, in $6p2\,^3P_2$ the BR effect was found to be practically non-existent, albeit with a tendency for a slight negative value. The 20 calculated values of λ in units of $\%\mathrm{fm}^{-2}$ were all $\in (-0.01119, 0.007393)$. Every series did not converge toward the experimental A in the ^{207}Pb reference isotope for this state as the active set was increased, so putting more weight on the $4th$ virtual layer is questionable. All the 20 expansions underestimated A in ^{207}Pb, and there was a clear trend observed where the greater the undershoot of A, the higher the corresponding value of λ. If only the calculated λ-values based on expansions that yielded a calculated A within $\pm 5\%$ of the experimental in ^{207}Pb are included, the interval reduces to $(-0.1119, -0.006998)$. Only three expansions achieved this accuracy and they were based on SD excitations from $6sp5sp4sp$ to one, two and four virtual layers, respectively. The series corresponding to SD excitations from $7s6sp5sp$ and S excitations from $7s6sp5sp4sp3sp2sp$ also approached the experimental A-value as virtual layers were added, although not reaching within 5% accuracy. Their corresponding λ-values also converged towards a similar range. For this reason, the value $\lambda(6p2\,^3P_2) = -0.009(4)\%\mathrm{fm}^{-2}$ is recommended. Again the uncertainty is chosen to extend twice the interval in question. This is a remarkably low value, and something that should be investigated in detail. It may indicate that the hyperfine anomaly due to the BR- and BW-effect is almost zero in $6p2\,^3P_2$, since their behavior is very similar.

In the final state considered, $6p2\,^1D_2$, all obtained values of λ were $\in (0.02907, 0.1220)$ in units of $\%\mathrm{fm}^{-2}$, with the greatest value being over four times the smallest. Here it is noted that λ takes the "wrong" sign, compared to theoretical prediction. These were the most scattered results obtained, incuding considerable deviation in λ within each series, as virtual layers were added. This is in accord with $6p2\,^1D_2$ being the state with the greatest range of calculated A-values in the ^{207}Pb reference isotope. For example, only 5 of the 20 obtained λ-values were based on expansions that yielded a calculated A within $\pm 5\%$ of the experimental in ^{207}Pb. Including only these 5, the interval reduces substantially to $(0.07750, 0.09633)$. If only those within $\pm 2.5\%$ of the experimental are included, another two values are excluded and the interval reduces further to $(0.09225, 0.09633)$. It is also observed that the series with the least deviation between the $1st, ..., 4th$ virtual layers, was the one based on allowing S substitutions from $6sp5sp4sp3sp2sp$, which was also the series with the most consistently accurate calculated A-values in the reference isotope. In the series including cv

and cc correlation there is some indication of convergence towards a value in the same range, but these results are not conclusive. Here more comprehensive calculations adding further virtual layers may be done to see if the calculated λ-values converge. Due to these facts, the value $\lambda(6p^2\,^1D_2) = 0.09(2)\%\text{fm}^{-2}$ is recommended.

In the end, this work strongly indicate that basing calculations of the BR-correction on an ASF that accurately reproduces the experimentally obtained value of the hfs constant A in the reference isotope is crucial. This was especially clear in $6p^2\,^1D_2$, where the wast range of obtained λ-values dramatically reduced when removing expansions corresponding to inaccurate A-values. Moreover, $6p^2\,^3P_1$ and $6p7s\,^3P_1$ had the most consistent calculated A-values near the experimental value in the ^{207}Pb reference isotope, and also the most consistent calculated proportionality constant λ. The same behavior is seen within series: where there was larger changes in the calculated A between virtual layers, there was larger changes in the calculated λ between virtual layers.

7.5.2   Effect of Expansion Size

Calculations based on several CSF expansions were done in order to gauge the importance of large CSF expansions in hyperfine anomaly calculations. The MCDHF method is computationally intensive, particularly for large systems with many electrons and as such it is of interest whether large, computationally expensive calculations are necessary.

The smallest expansion used to calculate the proportionality constant λ was the expansion consisting only of the multireference CSFs. When compared to the values obtained with electron correlation included, this led to calculated λ-values way off for all states in the $6p^2$ configuration, but spot on in the $6p7s$ configuration. In addition, for all states in the $6p^2$ configuration there was greater variance in the calculated λ-value within each series as the active set was increased, although there was a tendency for less change at the $4th$ virtual layer. To the contrary, in $6p7s\,^3P_1$ there were remarkably similar results from the $1st, ..., 4th$ virtual layer in all series.

The BR effect is mostly dependent on s and $p_{1/2}$ orbitals since these are the only ones with non-zero probability densities at the nucleus, which is required to affect the BR-correction to first order. The $6p^2$ configuration is more affected by electron correlation than $6p7s$, because it gets a mixing of CSFs containing "new" s-electrons, that alter the calculated λ-value. This effect is weaker in $6p7s$, since there already is an unpaired s-electron in the outer valence shell, and the BR effect is unaffected by the principal quantum number n of the s electron. It may be that an s-electron in the outer valence shell means smaller CSF expansions are required for calculations of the BR effect. This should however be studied in detail.

In conclusion, this work does not support the notion that large CSF expansions are necessary in general for calculations of the BR effect, as long as the calculated hfs constant A in the reference isotope is sufficiently converged towards the experimental value. This is in accord with what Heggset and Persson

[10] found in Hg. Here two expansions were used to calculate the BR effect between ^{199}Hg and other isotopes, and small differences in the results between the minimal and maximum expansions were found.

7.5.3 Variation in Skin Thickness

The largest absolute value of the proportionality constant τ in the linear fit $\tau \delta t$ for variations in the nuclear skin thickness was obtained from $\tau(6p^2\,^1D_2) = -0.0375\%\text{fm}^{-1}$. This entails an absolute change in the calculated hfs constant A of 0.00375% for each standard deviation (± 0.1fm) in the experimental value of t. This can be compared to the BR effect using $\lambda(6p^2\,^1D_2) = 0.09\%\text{fm}^{-2}$ and the maximum absolute deviation in mean squared radius for the isotope range, $|\delta \langle r_n^2 \rangle| = 1.466\text{fm}^2$, yielding a deviation of 0.13%. The difference in A caused by the skin thickness is then 2.8% of the BR effect. Similar calculations for the other states yield 2.9%, 2.5% and 2.9% of the BR effect, respectively.

Moreover, in the calculations of the BR effect, little impact on the calculated λ-values was observed when varying the skin thickness. Changes of $|\delta\lambda/\lambda_0| < 0.56\%$ were obtained for all calculations, with the single exception of $\delta t = -0.2$fm leading to $\delta\lambda/\lambda_0 = 3.6\%$ in $6p^2\,^3P_2$. For the four t-values 2.2fm, 2.3fm, 2.4fm and 2.5fm, $\delta\lambda/\lambda_0$ showed nice linearity in t for all states. However, for the value $t = 2.1$fm significant deviation was observed (max error $\delta\lambda/\lambda_0 = 3.6\%$ in $6p^2\,^3P_2$). Due to this deviation, the calculation for $t = 2.1$fm was ran twice to ensure no user mistake had been made in e.g. input to *rnucleus*. The identical result was obtained both times and the result is therefore believed to be correct. It is not known what causes the deviation, but it can be noted that for $t = 2.1$fm the coefficients of correlation for $6p^2\,^3P_2$ and $6p^2\,^1D_2$ were 0.9850 and 0.9998, while for all other skin-thickness calculations they were 0.9999.

If the values calculated for $\delta t = -0.2$fm are excluded, then all calculations led to deviations of $|\delta\lambda/\lambda_0| < 0.35\%$. This is one to two orders of magnitude smaller than the error in the determination of λ and can reasonably be disregarded. Even if the results obtained at $\delta t = -0.2$fm are correct, the maximum deviation of 3.6% in $6p^2\,^3P_2$ is still an order of magnitude smaller than the error in the determination of $\lambda(6p^2\,^3P_2)$.

All in all the presented work indicates that the skin thickness does not affect the BR effect a lot, as long as the skin thickness does not vary much between isotopes, and strengthen the belief that the linear fit $\lambda\langle r_n^2 \rangle$ represents the BR effect well, in accord with what Heggset and Persson [10] found in Hg.

7.5.4 Even and Odd Parity

Calculations were done based on SD excitations from $6sp$ and $6sp5sp$ to the $1st, ..., 4th$ virtual layer with even parity ($6p^2$) alone, and even ($6p^2$) and odd ($6p7s$) together. Of the eight values of λ obtained for each state, the greatest differences between the two calculations were $|\delta\lambda| \approx 0.77\%$ in $6p^2\,^3P_1$, $|\delta\lambda| \approx 437\%$

in $6p^2\,^3P_2$ and $|\delta\lambda| \approx 11\%$ in $6p^2\,^1D_2$. Some of the percentage wise deviations in $6p^2\,^3P_2$ are very large because of the small absolute value of $\lambda(6p^2\,^3P_2)$.

Overall, the obtained differences were often on the same order as the error in the determination of λ. This adds an additional source of uncertainty about the results obtained in this work, which should be kept in mind. Running odd and even together may be problematic based on these observations, which may be worth studying further.

7.5.5 Default Grid

One calculation was done based on expansions generated by allowing SD excitations from $6sp5sp$ to one,...,four virtual layers using both the default and the custom grid. The differences in the calculated values of the proportionality constant λ in the linear fit $\lambda\langle r_n^2\rangle$ for the BR effect between the grids were in most cases less than 1%, with the greatest difference being 2.38%. These deviations were one to four orders of magnitude smaller than the error in the determination of λ discussed in section 7.5.1, indicating that the default grid could have been used in the presented work without altering the obtained results by much.

However, it is clear that an error of order 1% could be relevant in certain cases. The great range of deviations obtained (smallest 0.00476% and biggest 2.38%) also makes it plausible that certain systems may experience even greater error. In the end, these results somewhat weaken the hypothesis that an extended grid is necessary for hyperfine anomaly calculations in heavy elements, unless high precision is needed. Choosing between grids ultimately comes down to the computational resources available and the required precision of the calculations.

7.5.6 Future Study

In the work presented, the most computationally expensive subprogram was in most cases *rmcdhf*. The TF-approximation was used to give initial estimates of the radial orbitals in the scf procedure at every step. Quicker convergence was achieved by using the radial orbitals obtained for an adjacent value of R as initial estimates, but this led to unintelligible results where $\delta A/A_0$ showed no semblance of linearity in R. This may be due to errors in the wavefunctions, perhaps because the program finds a local minimum. It is not known whether this is an artifact of the system considered here, or a general problem in GRASP2018. Further exploration in other systems may be worthwhile as the potential computational savings are very significant. For example, for the largest CSF expansion used as basis for a BR-calculation (SD excitations from $7s6sp5sp4sp$ to four virtual layers), convergence of the $4th$ virtual layer was reached after 40 to 43 iterations, for the various nuclear models, when starting from TF functions. The run-times were then in excess of 34 hours for each data point. Having to do this once and not ten times would save ≈ 300 hours if the nine remaining data points converged after two iterations.

Another way to reduce the computational cost in BR-calculations may be to reduce the number of data points. The coefficients of correlation were generally very high (see Appendix A), providing assurance of the strength of the linear relationship. This indicates that 10 data points were unnecessary in this work, as removing e.g. every other data point would lead to a very slight modification of the obtained λ-values.

In the end, a lot of unnecessary calculations were carried out. Many calculations of the BR effect were done, some of whom provided poor results. More time ought to have been spent finding expansions that better reproduced the experimental A-values in the ^{207}Pb reference isotope, rather than doing quite so many calculations of the BR effect.

WARNING. Just as the CSFs generated by allowing S substitutions represent polarisation of the CSFs in the multireference, CSFs generate by allowing SD substitutions represent polarization of the important corresponding to S substitutions.

WARNING. The series based on SD substitutions from $6sp5sp$ seemed promising in $6p^2\,^1D_2$, and could perhaps have been extended with further virtual layers. It is possible that this would have led to even better results.

Chapter 8

Conclusion

The Breit-Rosenthal (BR) effect between [207]Pb and other isotopes was calculated in a parametric study using a two-parameter Fermi nuclear model where the mean squared radius $\langle r_n^2 \rangle$ was varied. The hyperfine structure constant was calculated numerically for the states $6p^2\ ^3P_{1,2}$ and $^1D_2$ and $6p7s\ ^3P_1$ using the multi-configuration Dirac-Hartree-Fock method with the GRASP2018 software package [5].

The proportionality constant λ in the linear fit $\lambda \langle r_n^2 \rangle$ for the BR effect was calculated for 20 CSF expansions of various sizes, using an extended grid as recommended for heavy elements by [4] and [12]. The work presented indicates that a high number of CSFs in the expansion is not crucial, as long as the expansion accurately reproduces the experimentally obtained A in the reference isotope. The recommended λ-values based on this work are given in table 8.1.

State	$6p^2\ ^3P_1$	$6p^2\ ^3P_2$	$6p^2\ ^1D_2$	$6p7s\ ^3P_1$
$\lambda[\%\,\mathrm{fm}^{-2}]$	-0.083(2)	-0.009(4)	0.09(2)	-0.065(3)

Table 8.1: Recommended values for the proportionality constant λ in the linear fit $\lambda \langle r_n^2 \rangle$ for the BR effect, based on this work.

Moreover, calculations were done varying the nuclear skin thickness by ± 0.1fm and $+0.2$fm from the default value 2.3fm. Resulting deviations in the calculated λ were an order of magnitude or more less than the uncertainty in the determination of λ. It is therefore believed that the skin thickness does not affect the BR effect much, as long as the skin thickness does not vary much between isotopes, indicating that the linear fit $\lambda \langle r_n^2 \rangle$ is a good approximation for the BR-effect.

Chapter 9

Sammendrag på Norsk

Atomer er grunnleggende byggeklosser for materie, bestående av en atomkjerne med protoner og nøytroner, og en sky av elektroner som omslutter den. Studie av atomers egenskaper er av interesse både for fundamental forskning og teknologiske anvendelser. Én egenskap av interesse er atomkjernens magnetiske moment, som kan måles direkte ved høy-resolusjon spektroskopiteknikker som kjernemagnetisk resonans (NMR). Dette er dog ikke mulig for tilstrekkelig ustabile isotoper, fordi det krever en viss levetid for atomkjernen. I stedet må indirekte metoder brukes, for eksempel studie av hyperfinstrukturen.

I atomer er elektronene tvunget til å være i spesifikke, diskré energinivåer, som beskrevet av kvantemekanikk. Hyperfinstrukturen er små splittinger av disse tillatte energinivåene i flere veldig nærliggende nivåer som resulterer av svake elektriske og magnetiske vekselvirkninger mellom atomkjernen og elektronskyen. Det magnetiske momentet i atomkjerner med kort levetid kan finnes fra spektroskopiske målinger av hyperfinstrukturen, når disse sammenlignes mellom den ustabile isotopen og en mer stabil referansenuklide med kjent magnetisk moment. Disse beregningene involverer forholdet mellom magnetisk dipol hyperfinstrukturkonstantene A_1 og A_2 i de to nuklidene. Dette forholdet kan ikke bestemmes eksakt på grunn av den såkalte differensielle hyperfine anomalien, som skyldes den forskjellige størrelsen til atomkjernene. Noe av usikkerheten grunnet denne anomalien kan fjernes ved å beregne noen korreksjoner, inkludert Breit-Rosenthal (BR) korreksjonen grunnet distribusjonen av elektrisk ladning i de to kjernene.

Denne rapporten presenterer beregninger av Breit-Rosenthal (BR) korreksjonen til hyperfin anomalien for tilstandene $6p^2\,^3P_1, ^3P_2$ og $^1D_2$, og $6p7s\,^3P_1$ mellom ^{207}Pb og andre isotoper. Disse ble beregnet numerisk med multikonfigurasjon Dirac-Hartree-Fock (MCDHF) metoden ved bruk av programpakken General Relativistic Atomic Structure Package 2018 (GRASP2018) [5]. Atomkjernen ble modellert ved en to-parameter Fermi-distribusjon, hvor BR-effekten ble approsimert ved variasjon i middel kvadrert radius $\langle r_n^2 \rangle$. Fermifordelingen er

$$\rho(r) = \frac{\rho_f}{1 + e^{(r-c)/a}},$$

der c er halv-tetthet radien slik at $\rho(c) = \frac{1}{2}\rho(0)$ og a er en diffusitetsparameter relatert til hudtykkelsen t ved $t = a \cdot 4ln3$ [15, p. 5].

GRASP2018 er basert på approksimerte, relativistiske bølgefunksjoner kalt atomtilstandfunksjoner (ASFs), hvor de gode kvantetallene er paritet P og total dreieimpuls J. Disse er lineærkombinasjoner av dreieimpulskoplede basistilstander, såkalte konfigurasjonstilstandfunksjoner (CSFs), som i seg selv også er egentilstander av paritet og total dreieimpuls. Disse blir bygt opp av antisymmetriserte produkter av én-elektron Dirac spin-orbitaler, som er generelle løsninger av Dirac-ligningen i et sentralfelt. En fullstendig relativistisk behandling basert på Dirac-ligningen er særlig viktig i tunge atomer, hvor relativistiske effekter er store. Elektronkorrelasjon utover sentralfelt-approsimasjonen inkluderes ved å ta med CSFs som korresponderer til et videre utvalg av elektronkonfigurasjoner med passende vekting. Atomtilstandfunksjonene kan da skrives

$$|\Gamma P J M_J\rangle = \sum_{i=1}^{N_{csf}} c_{\Gamma_i} |\Gamma_i P J M_J\rangle,$$

der N_{csf} er antall CSFs i ekspansjonen, c_{Γ_i} er ekspansjonskoeffisientene og Γ representerer alle andre kvantetall som trengs for å unikt identifisere tilstanden. Gitt en CSF basis, optimeres ekspansjonen med MCDHF metoden der variasjonsprinsippet brukes med hensyn på variasjoner i orbitalene og ekspansjonskoeffisientene. Energifunksjonalen konstrueres med den approsimerte, såkalte Dirac-Coulomb (DC) Hamiltonoperatoren

$$\hat{H}_{\mathrm{DC}} = \sum_{i=1}^{N} \left[c\boldsymbol{\alpha}_i \cdot \mathbf{p}_i + (\beta_i - I_4)c^2 + \hat{V}_n(r_i) \right] + \sum_{i=1}^{N} \sum_{i<j} \frac{1}{r_{ij}},$$

der én-elektron operatorene er de relativistiske Dirac-operatorene, mens to-elektron operatorene approsimeres ved Coulomb frastøtning. I basisen av orbitalene opptimert med MCDHF metoden basert på DC Hamiltonoperatoren, kan ekstra korreksjoner legges til i en konfigurasjonsvekselvirkning. Her optimeres ekspansjonskoeffisientene ved å først diagonalisere Hamiltonmatrisen og løse egenverdiproblemet $\mathbf{Hc} = E\mathbf{c}$, der de nye egenvektorene korresponderer til de opdaterte ekspansjonskoeffisientene. I GRASP2018 legges Breit korreksjon og korreksjoner fra kvanteelektrodynamikk (QED) til på denne måten. Gitt en ferdig optimert ASF, kan observerbase størrelser beregnes fra denne.

I det utførte arbeidet ble hyperfinstrukturkonstantene i de fire nevnte tilstandene beregnet for 10 forskjellige radier i Fermi-fordelingen. Variasjon i middel kvadrert radius $\langle r_n^2 \rangle$ korresponderte til hele isotopbredden til bly, basert på data fra Angeli og Marinova [1]. Forskjellen i beregnet A sammenlignet med referanseradien $\delta A/A_0$ for de 10 datapunktene ble beregnet sammen med proporsjonalitetskonstanten λ i den lineære tilpasningen $\lambda\langle r_n^2 \rangle$. En slik beregning

av λ ble gjort basert på 20 forskjellige CSF ekspansjoner av varierende størrelse og medfølgende krav til datakraft. GRASP2018 ble kompilert med en utvidet grid, som anbefalt for tunge, nøytrale atomer av [4] og [12]. De anbefalte verdiene for λ i de fire tilstandene basert på dette arbeidet er gitt i tabell 9.1

State	$6p^2\,{}^3P_1$	$6p^2\,{}^3P_2$	$6p^2\,{}^1D_2$	$6p7s\,{}^3P_1$
$\lambda[\%\,\text{fm}^{-2}]$	-0.083(2)	-0.009(4)	0.09(2)	-0.065(3)

Table 9.1: Anbefalte verdier for proporsjonalitetskonstanten λ i den lineære tilpasningen $\lambda\langle r_n^2\rangle$ for BR-effekten, basert på det presenterte arbeidet.

Resultatene indikerer at ett s-elektron i det ytre valensskallet gjør at mindre CSF ekspansjoner er nødvendig for beregninger av hyperfin anomali. Dette er dog noe som bør studeres nøyere. Generelt indikerer arbeidet at store CSF ekspansjoner ikke nødvendigvis trengs for beregninger av hyperfin anomali så lenge god konvergens mot de eksperimentelt observerte verdiene av hyperfin-struktur konstanten A i referanseisotopen er oppnådd.

Videre ble beregninger utført der hudtykkelsen t til atomkjernen ble variert med ±0.1fm og $+0.2$fm fra referanseverien 2.3fm. Dette tilsvarer ett og to standardavvik i verdiene funnet ved å tilpasse Fermi-parameterene til eksperimentelle spredningsdata [3, p. 31-36]. De resulterende variasjonene i de beregnede λ var minst én størrelsesorden mindre enn usikkerheten i bestemmelsen av λ basert på variasjon i radien. Det er derfor trolig at hudtykkelsen ikke påvirker BR-effekten mye, så lenge hudtykkelsen ikke varierer mye mellom isotopene, noe som indikerer at den lineære tilpasningen $\lambda\langle r_n^2\rangle$ er en god approksimasjon for BR-effekten.

Bibliography

[1] István Angeli and Krassimira Petrova Marinova. Table of experimental nuclear ground state charge radii: An update. *Atomic Data and Nuclear Data Tables*, 99(1):69–95, 2013.

[2] S Büttgenbach. Magnetic hyperfine anomalies. *Hyperfine Interactions*, 20(1):1–64, 1984.

[3] L R B Elton. *Nuclear Sizes*. Oxford University Press, 1961.

[4] J Bieroń et al. *A practical guide to GRASP2018 - A collection of Fortran 95 programs with parallel computing using MPI*. The Computational Atomic Structure group, 2018.

[5] C Froese Fischer, Gediminas Gaigalas, Per Jönsson, and Jacek Bieroń. Grasp2018—a fortran 95 version of the general relativistic atomic structure package. *Computer Physics Communications*, 237:184–187, 2019.

[6] Charlotte Froese Fischer, Michel Godefroid, Tomas Brage, Per Jönsson, and Gediminas Gaigalas. Advanced multiconfiguration methods for complex atoms: I. energies and wave functions. *Journal of Physics B: Atomic, Molecular and Optical Physics*, 49(18):182004, 2016.

[7] Charlotte Froese-Fischer, Tomas Brage, and P Johnsson. *Computational atomic structure: an MCHF approach*. CRC press, 1997.

[8] Ian P Grant. *Relativistic quantum theory of atoms and molecules: theory and computation*. Springer, 2007.

[9] David J Griffiths and Darrell F Schroeter. *Introduction to quantum mechanics*. Cambridge university press, 2018.

[10] Tarjei Heggset and Jonas R Persson. Calculation of the differential breit–rosenthal effect in the 6 s 6 p 3 p 1, 2 states of hg. *Atoms*, 8(4):86, 2020.

[11] Walter R Johnson. *Atomic structure theory*. Springer, 2007.

[12] Per Jönsson, Gediminas Gaigalas, Jacek Bieroń, C Froese Fischer, and IP Grant. New version: Grasp2k relativistic atomic structure package. *Computer Physics Communications*, 184(9):2197–2203, 2013.

[13] Per Jönsson, Michel Godefroid, Gediminas Gaigalas, Jörgen Ekman, Jon Grumer, Wenxian Li, Jiguang Li, Tomas Brage, Ian P Grant, Jacek Bieroń, et al. An introduction to relativistic theory as implemented in grasp. *Atoms*, 11(1):7, 2022.

[14] Per Jönsson, Farid A Parpia, and C Froese Fischer. Hfs92: A program for relativistic atomic hyperfine structure calculations. *Computer physics communications*, 96(2-3):301–310, 1996.

[15] Ann-Marie Mårtensson-Pendrill. Atoms through the looking glass-a relativistic challenge. *Can. J. Phys*, 99:1–16, 2007.

[16] Jonas R Persson. Table of hyperfine anomaly in atomic systems. *Atomic Data and Nuclear Data Tables*, 99(1):62–68, 2013.

[17] JR Persson. Hyperfine structure and hyperfine anomaly in pb. *Journal of Physics Communications*, 2(5):055028, 2018.

[18] IAEA Nuclear Data Section. Nuclear electromagnetic moments. `https://www-nds.iaea.org/nuclearmoments/`, 2022.

[19] Magnus Själander, Magnus Jahre, Gunnar Tufte, and Nico Reissmann. EPIC: An energy-efficient, high-performance GPGPU computing research infrastructure, 2019.

Appendix A

All Data

Table A.1 gives the proportionality constant λ in the linear fit $\lambda\langle r_n^2\rangle$ for the BR effect, calculated with all the 20 CSF expansions discussed in chapter 7, along with the corresponding coefficients of correlation.

State	$\lambda^{(1)}[\%\ \mathrm{fm}^{-2}]$	R_0^2	$\lambda^{(2)}[\%\ \mathrm{fm}^{-2}]$	R_0^2	$\lambda^{(3)}[\%\ \mathrm{fm}^{-2}]$	R_0^2	$\lambda^{(4)}[\%\ \mathrm{fm}^{-2}]$	R_0^2
SD excitations from $7s6sp$								
$6p^2\ ^3P_1$	-0.08396743	0.9999	-0.08487621	0.9999	-0.08551977	0.9999	-0.08558785	0.9999
$6p^2\ ^3P_2$	-0.00349586	0.9999	-0.00398155	0.9999	-0.00303264	0.9999	-0.00326937	0.9999
$6p^2\ ^1D_2$	0.09063272	0.9999	0.09784377	0.9999	0.10503671	0.9999	0.10369977	0.9999
$6p7s\ ^3P_1$	-0.06579227	0.9999	-0.06678529	0.9999	-0.06718759	0.9999	-0.06706637	0.9999
SDT excitations from $7s6sp$								
$6p^2\ ^3P_1$	-0.08519381	0.9999	-0.08603834	0.9999	-0.0866651	0.9999	-0.08672204	0.9999
$6p^2\ ^3P_2$	-0.00140463	0.9998	-0.00127042	0.9998	-0.00090658	0.9997	-0.00114026	0.8433
$6p^2\ ^1D_2$	0.10283301	0.9999	0.11376507	0.9999	0.12200859	0.9999	0.12044316	0.9999
$6p7s\ ^3P_1$	-0.06587667	0.9999	-0.0668977	0.9999	-0.06746665	0.9999	-0.06803119	0.9998
SD excitations from $7s6sp5sp$								
$6p^2\ ^3P_1$	-0.08781368	0.9999	-0.08249784	0.9999	-0.08420331	0.9999	-0.08363947	0.9999
$6p^2\ ^3P_2$	0.00739268	0.9999	-0.00634062	0.9999	-0.00383911	0.9999	-0.00599735	0.9999
$6p^2\ ^1D_2$	0.0611288	0.9999	0.06967400	0.9999	0.08556362	0.9999	0.08549159	0.9999
$6p7s\ ^3P_1$	-0.0661692	0.9999	-0.06510511	0.9999	-0.06533601	0.9999	-0.06566834	0.9999
SD excitations from $7s6sp5sp4sp$								
$6p^2\ ^3P_1$	-0.07858507	0.9999	-0.07967823	0.9999	-0.0841265	0.9999	-0.08252524	0.9996
$6p^2\ ^3P_2$	-0.01049925	0.9980	-0.01119126	0.9997	-0.00442032	0.9988	-0.00699838	0.9929
$6p^2\ ^1D_2$	0.02907244	0.9984	0.04951961	0.9997	0.07360763	0.9999	0.06529916	0.9988
$6p7s\ ^3P_1$	-0.06532802	0.9999	-0.06467919	0.9999	-0.06537086	0.9999	-0.06532425	0.9999

S excitations from $7s6sp5sp4sp3sp2sp$							
$6p^2\,{}^3P_1$	-0.08105163	0.9999	-0.08386854	0.9999	-0.08373628	0.9999	-0.08325832	0.9999
$6p^2\,{}^3P_2$	-0.00718057	0.9999	-0.0037402	0.9999	-0.00402268	0.9999	-0.00497682	0.9999
$6p^2\,{}^1D_2$	0.0775033	0.9999	0.0951952	0.9999	0.09632899	0.9999	0.09225253	0.9999
$6p7s\,{}^3P_1$	-0.06241899	0.9999	-0.06404879	0.9999	-0.06382963	0.9999	-0.06375163	0.9999

Table A.1: The proportionality constant λ in the linear fit $\lambda\langle r_n^2\rangle$ for the BR effect. The values in each column correspond to substitutions to one, two, three and four virtual layers, i.e. $\lambda^{(N)}$ is the value calculated for the expansion based on allowing excitations to N virtual layers. Extended grid only.